Motion Control
of Industrial Printers

Master's Thesis

Tim Klaassen
DCT Report nr. 2002.11
February 19, 2002

Exam date: March 5, 2002

Committee: Prof. dr. ir. M. Steinbuch
Prof. dr. ir. P.P.J. van den Bosch
Dr. ir. M.G.E. van den Molengraft
Dr. ir. E. Homburg
Ir. M.J. Smallegange

Professor: Prof. dr. ir. M. Steinbuch

Coaches: Ir. M.J. Smallegange
F.A. Engels

Eindhoven University of Technology
Department of Mechanical Engineering
Section of Dynamics and Control Technology

creased without loosing accuracy, the performance of the Linear Drive Unit is investigated.
The dynamical model shows that varying the capstan radius and transmission wheel radius has a non-linear effect on the process gain and the position of eigenfrequencies.
Identification of the process Frequency Response Function shows several damped resonances which are due to the printheads and other features mounted at the LDU.
With the present controller used at the Linear Drive Unit, a closed loop bandwidth of 8 [Hz] is obtained. The gain margin is 2 [dB]. By using a lead-lag controller with two notches to reduce the effect of resonances and a second order low-pass filter to reduce measurement noise, the closed loop bandwidth can be increased to 50 [Hz], with enough gain and phase margin.

Abstract

To give Stork Digital Imaging insight in how to use control systems to optimize performance and to reduce the costs of the products, two case studies are performed. The first is a feasibility study for increasing performance and robustness of the Image Verification Unit (IVU). The second study investigates the performance of the Linear Drive Unit (LDU) to optimize the image quality of the AX-series printers.

The Image Verification Unit is part of the Amethyst textile printer. Its task is to print and scan an image on paper to calibrate the printheads. In the current design problems arise with positioning the image in front of the scan position. This is due to the varying tension force in the paper. With this varying tension force, also the path length from print to scan position varies. Because the controller does not measure and feed back the paper position, the paper can not be positioned within a certain margin. A new system is proposed which uses two DC motors to control the tension and position the paper. The paper position is estimated by measuring a capstan rotation.
A dynamical model is derived to show the non-linear behavior due to varying reel radii during tape transport. The controller consists of a feedforward tension controller, a position controller and friction compensation.
A prototype is build using two switch-mode drivers to drive the DC motors, a quadrature encoder to measure the capstan rotation and two optical sensors to measure the reel rotations. The experimental setup uses a data acquisition system which runs in real-time from within Matlab by using Wintarget.
Process identification shows a Frequency Response Function similar to the derived model. Friction identification shows a Stribeck behavior. Using a Proportional-Differential controller, a robust stable closed loop system is obtained. Experiments show that the redesign improved the performance of positioning 10 times.

The task of the Linear Drive Unit, part of the AX-series proofers, is to position the print cassettes in front of the drum. The translation is obtained by rotating a capstan over a guide bar strip. The position of the printheads is estimated by measuring the rotation of the capstan. Due to mechanical deviations, the position estimation differs from the real position. This error causes a deviation in the color spectrum of a grey-image.
A thorough error analysis shows that the positioning errors originate from various sources. Varying capstan radius, capstan bearing misalignment, capstan bearing eccentricity, encoder mounting eccentricity and encoder bearing eccentricity all result in a systematic error with a wavelength equal to the capstan circumference. Variations in the guide bar strip thickness also acts as a significant disturbance, as the path length depends on this thickness. Dirt and slip in the system also cause direct measurement errors. Quantization of the measurement error and the color spectrum shows a large coherence at three wavelengths. To eliminate all measurement errors, it is recommended to use a direct measurement system.
With a view to increasing printer productivity, where the speed of positioning must be in-

Table of Contents

Chapter 1

General Introduction

Stork Digital Imaging produces high end textile and graphic printers. The systems currently under development are the Amethyst (textile), the AX-series (graphic) and the Eagle (graphic). These printers use a dot size modulation inkjet technology. This means that every pixel is composed of different numbers of ink droplets. The number of droplets in a pixel determines the dot size that make the lighter and darker shades of color. All printers use the colors Cyan, Magenta, Yellow and Black (CMYK). The Amethyst uses also orange, blue golden-yellow and red to extend the color-space on textile. The print resolution of the Amethyst is 10 pixels per mm. The AX-series and the Eagle print at a resolution of 12 or 24 pixels per mm.

The Amethyst and AX-series are both continuous ink jet printers. This means that the nozzles produce a jet of ink at a constant rate of 625000 drops per second. Each drop is then electrostatically charged depending on the pixel data requirements. The charged droplets are deflected in flight by an electrical field, so the drops can be placed on the substrate or the ink can be recycled. The Amethyst uses a Multi Level Deflection technology, where each drop can be deflected to 5 lines. A schematic view of this principle is shown in figure 1.1. The main advantage of this method is that each drop has exactly the same volume, resulting in an evenness of tone and color in the final print. The Eagle uses a drop on demand ink jet technology. This means that the nozzle is excited depending on the print data. Every drop of ink that leaves the nozzles is placed on the paper.

The Amethyst prints on pre-treated textile of up to 1600 [mm] in width. It uses the Substrate Handling Unit and the Linear Motion Unit to build up a print. The principle used is like an ordinary desk-jet printer. The Substrate Handling Unit places the substrate in front of

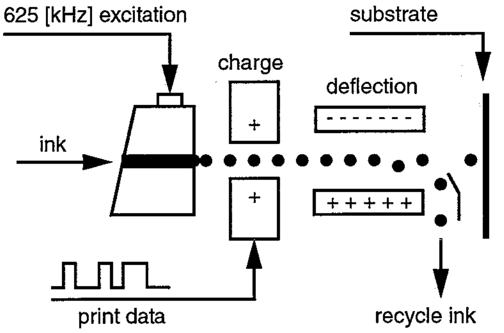

Figure 1.1: Continuous ink jet principle

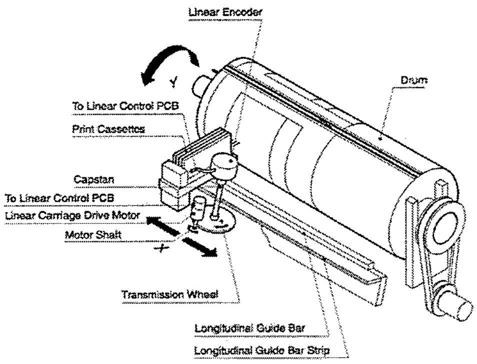

Figure 1.2: Image build-up at the AX-series and Eagle

the printheads. The Linear Motion Unit moves the printheads horizontally in front of the substrate at constant velocity. Every stroke of these printheads, a width of 8 [mm] is printed. If one stroke is printed, the substrate is moved 8 [mm], so the next stroke can be printed. The image build-up at the AX-series and the Eagle is different from a desk-jet printer. The substrate is stretched onto a drum. During printing, the Drum Unit maintains a constant rotation speed. The printheads are positioned in front of the drum by the Linear Drive Unit (figure 1.2). If a stroke is printed, the Linear Drive Unit steps to the next position.

When designing modern high quality applications or products like the Stork printers, it is important to obtain high performance, but on the other hand low costs. When using smart control strategies to control a process, it might be possible to achieve this. This research project has the goal to give Stork Digital Imaging insight in how to use control systems to optimize performance and to reduce the costs of the products. In this framework two case studies are performed.

The first study is part of a project to increase reliability of the Amethyst textile printer. The printheads of this system are calibrated automatically. If this calibration is not performed accurately, it has a significant effect on the image quality. The Image Verification Unit carries out a considerable part of this process. The task of this unit is to print an image on a paper roll, and to position this image in front of a CCD-camera where the image is scanned. This scan information is used for calibrating the printheads. In the present design, problems arise with positioning the image in front of the camera. Part I of this report describes a feasibility study for increasing performance and robustness of the Image Verification Unit (IVU).

The second study is coherent to the image quality of the AX-series proofer. A measure of this quality is the consistency of a grey-image. A grey-image is an image of which each pixel contains one ink drop of each color. This image is the most sensitive to deviations in the size and position of the droplets. The color spectrum of this print shows large deviation and a periodic pattern in the error. The proofer only passes the quality test if the color deviation is within a certain margin. The most significant disturbance is a ±19 [mm] pattern. This wavelength can be reduced to the performance of the Linear Drive Unit. The capstan circumference is namely also ±19 [mm]. In part II the coherence between the grey-image quality and the performance of the printheads is investigated. To minimize the effect of the Linear Drive Unit mechanics on the image quality, a new, direct measurement system is proposed. With a view to increasing printer productivity, where the speed of positioning must be increased without loosing accuracy, the performance of the Linear Drive Unit is analyzed and some optimizations are proposed.

Part I

Redesign of the Image Verification Unit

Chapter 2

Introduction

The Image Verification Unit is part of the Amethyst textile printer produced by Stork Digital Imaging. Its task is to print and scan an image on a paper roll, which is used for calibrating the printheads. The IVU can be separated into two parts, the image handling and the paper handling or motion part.

The motion part of the Image Verification Unit, shown in figure 2.1, consists of two reels and a capstan. Each reel is coupled to a DC motor by a slip coupling. The purpose of these motors is to keep the tape under tension. The translation of the tape is realized by the capstan, which is driven by a stepping motor. To move the image from the printing area to the scanning area, the stepper motor is set to step a certain distance. To control the paper translation, an open loop controller is used. If the effective path length from printing to scanning area is constant, the image will be positioned accurate in front of the CCD camera each movement. However, here lies the problem of positioning. Because the slip couplings are set to a constant torque, the tension force in the paper changes as the paper roll radii changes. The effective length of the tape path relates to this tension force of the tape, hence also the path length changes. As a result, the image is not positioned accurate in front of the camera, and it is not possible to calibrate the printheads accurately.

In this report a redesign of the current system is described, which uses two DC motors to drive the reels. These motors can be used for both positioning the image and keeping a constant tension force in the paper. In chapter 3 we will describe the redesign concept. Then first a

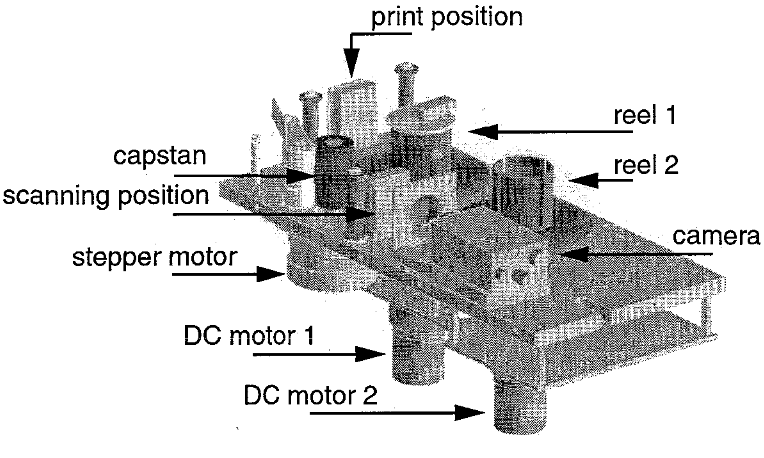

Figure 2.1: Present IVU system

dynamic model is derived (chapter 4). In chapter 5 a stabilizing controller is designed. To check whether the concept would work in practise, this model including controller is simulated using Simulink, which is described in chapter 6. A prototype is build to test the system in practise. Chapter 7 describes the practical setup. Using this system, the process parameters are identified (chapter 8). Here also the test results are described. We finalize this study with some conclusions and recommendations in chapter 9.

Chapter 3

Redesign Concept

The main reason for redesigning the IVU motion system is that in the current setup problems occur with positioning the image in front of the camera. The paper cannot be positioned within a certain margin. Cause of this error is that the effective tape length (length from print to scanning position) depends on the tension force in the paper. Because the paper has a radial stiffness, we need a certain force to bend the paper around the guidance rolls. The torque applied by the slip couplings at the reels is set to a constant value. Because the paper roll radius change during tape transport, the tension force in the paper also changes, hence the effective tape length is not constant. The current system does not use a control loop to position the image, but is an open loop drive. The drive sequence (the number of steps of the stepper motor) is chosen constant. Together with the varying effective tape path this means that the total step distance changes. The camera window has a margin of ± 0.5 [mm]. In the current setup, the image is positioned with an accuracy of ± 1 [mm], which is clearly not enough. With the new system the goal is to minimize the positioning error, and stay within the camera window. The speed of positioning is not of importance, but has to be comparable with the current speed, which is set to approximately 0.02 [m/s].
Another problem is that the slip couplings are under large wear and tear. It is then likely not to use these couplings in a new design. A third problem is that the current system is very expensive. A new design must therefor also reduce the costs. From this we can set out some goals to achieve with the redesign:

- improve positioning accuracy for complete range of reel radii
- obtain higher durability
- reduce the system costs

We will propose three solutions which handle these problems and discuss their advantages and disadvantages.

1. **Different guiding system**
   Because of the radial stiffness of paper, a large tension force is needed to tighten the paper around a guidance roll with small radius. At the current system the tension force is not constant due to the change in reel radii. It may be possible to use a different

guidance system to avoid these sharp corners and keep the tape length more or less constant at varying tension force. This would be a relative simple solution as only the layout is changed. A disadvantage is that the space available is not adequate for changing the paper handling. Also the durability is not increased as the slip couplings are not eliminated. The system costs would remain the same, because the same parts are used only in a different layout.

2. **Use CCD camera to position the image**
   If the print image is changed in such way that the camera can detect the beginning of the image, it is possible to use this information to stop the movement at the right position. To be able to do this, we must be certain that the printheads are aligned and working properly to guarantee a repeatable image which can be recognized. This is not the case, because then the IVU would not be needed. Another problem here is that when the stepper motor is used for translation of the paper, the paper trembles a lot and it is not possible to scan the image. If the translation is stopped each step to check wether the image is at the right position, the speed of positioning would be limited too much. Also, as in the previous solution, the durability is not increased as the slip couplings are not eliminated.

3. **Use two direct drive DC motors to control tension force and positioning**
   By using two direct drive DC motors to drive the reels, from which one is used for positioning the paper and the other is used to keep the paper under tension, the torque can be varied to achieve a constant tension force in the paper. If the tape translation is measured, it is possible to achieve an accurate positioning by using a feedback control loop. An advantage of this system is that durability is increased and costs are decreased with removing the slip couplings and the stepper motor. Of course, this setup requires a controller and an encoder to measure the position, which will increase the costs.

If we look at the project goals, the last solution is the most interesting. Systems like tape and video recorders use the same method and have also proven to be accurate and robust [1]. A feasibility study will be done to check wether this system shows to be reliable and robust using low-cost system parts.

Chapter 4

Modelling

In order to design control algorithms for positioning the printed image in front of the CCD camera, a model of the IVU motion system has to be made. In figure 4.1 a schematic overview of the IVU is presented. It consist of two direct drive DC motors, two couplings which connect the motors to the reels, two reels, paper and a capstan. Sensors are present at both reels and at the capstan. When moving the image from the print position to the scanning position, the paper rolls from reel 1 via the capstan to reel 2. Due to the mechanical layout, during this movement the angular velocities of the capstan, reel 1 and motor 1 are negative, but the angular velocities of reel 2 and motor 2 are positive.
The direct drive DC motors are modelled by inertias J_{m_i}, which are driven by torques τ_i. The couplings are modelled as torsion spring and dampers with stiffness c_{m_i} and damping k_{m_i}. The reels and capstan are modelled as inertias. The coupling of the capstan to both of the reels by the paper is modelled as a linear spring and damper system with stiffness c_i and damping constant k_i. The mass of the paper is negligible between the two reels, but it is considered to have a certain thickness d_{tape}, height h_{tape} and density ρ_{tape} when rolled up on the reels. This causes the reel mass and diameter to change during tape transport.
When looking at the dynamics of the IVU motion system, we can divide it into two parts, a non-linear dynamic behavior of the tape drive system, which is caused by the fact that the inertias of the reels change during tape transport, and a linear behavior, which describes the

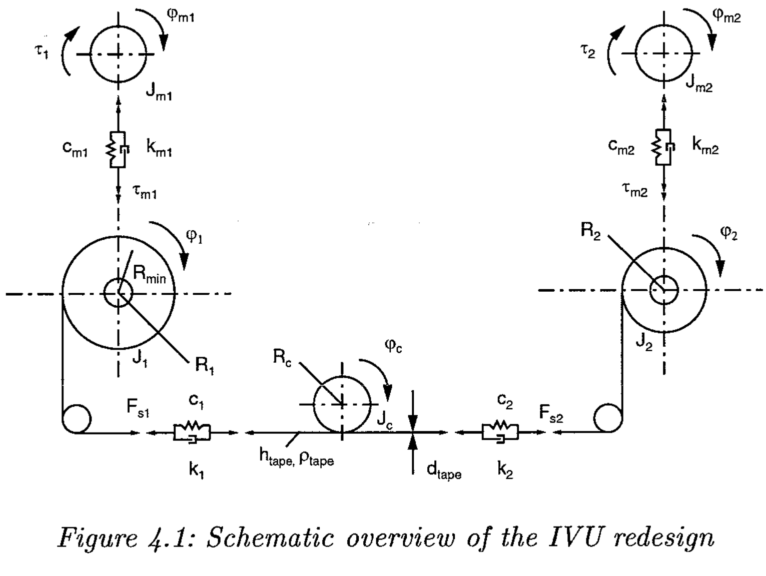

Figure 4.1: Schematic overview of the IVU redesign

rotations, paper translations and spring and damper deflections. In the model to be described both effects are taken into account. We will now first describe the changes in inertia and then derive the relevant dynamical model.

4.1 Reel inertia

In general, the inertias of a cylinder can be described by the following equation:

$$J = \frac{1}{2}m(R^2 + R_{min}^2)$$

and

$$m = \pi\rho h(R^2 - R_{min}^2)$$

For the two reels including the paper roll this gives:

$$J_1 = J_{1_0} + \frac{\pi}{2}\rho_{tape}h_{tape}(R_1^4 - R_{min}^4) \tag{4.1}$$

$$J_2 = J_{2_0} + \frac{\pi}{2}\rho_{tape}h_{tape}(R_2^4 - R_{min}^4) \tag{4.2}$$

where J_{1_0} and J_{2_0} are the inertias of the reels without paper.
Calculation of R_1 and R_2 gives:

$$R_1 = R_{min} + \frac{d_{tape}}{2\pi}\varphi_1 \tag{4.3}$$

$$R_2 = R_{min} + \frac{d_{tape}}{2\pi}\varphi_2 \tag{4.4}$$

The speed by which the radii change:

$$\frac{\partial R}{\partial t} = \frac{\partial R}{\partial \varphi}\frac{\partial \varphi}{\partial t}$$

gives

$$\dot{R}_1 = \frac{d_{tape}}{2\pi}\dot{\varphi}_1 \tag{4.5}$$

$$\dot{R}_2 = \frac{d_{tape}}{2\pi}\dot{\varphi}_2 \tag{4.6}$$

The speed by which the inertias change:

$$\frac{\partial J}{\partial t} = \frac{\partial J}{\partial R}\frac{\partial R}{\partial t}$$

gives

$$\dot{J}_1 = 2\pi\rho_{tape}h_{tape}R_1^3\dot{R}_1 \tag{4.7}$$

$$\dot{J}_2 = 2\pi\rho_{tape}h_{tape}R_2^3\dot{R}_2 \tag{4.8}$$

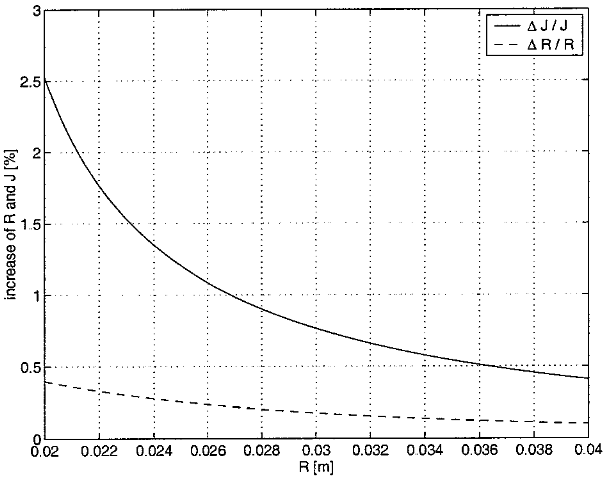

Figure 4.2: Increase of R and J during one operation ($\Delta x = 0.2$ [m])

The step size during one movement is limited to $\Delta x = 0.2$ [m]. Together with the paper parameters and equation (4.1) to (4.8), we can quantify the change in reel radii and inertias. Figure 4.2 shows the percentage of change in inertia over the complete range of reel radii within one movement. We see that the maximum change in inertia is only 2.5% at $R_i = 20 \cdot 10^{-3}$ [m]. The change in reel radius is even smaller, hence we will further neglect this non-linear phenomenon and assume the inertias and reel radii to be constant in each operating point. This means that locally we take $\dot{J}_i = 0$ and $\dot{R}_i = 0$. Globally equations (4.5) to (4.8) are still valid.

4.2 Dynamics

Before we can derive the dynamical model, we make a few assumption:

- the dynamics of the motor electronics can be ignored
- the friction at the reels and capstan can be neglected
- because of low angular velocities, the friction at servo motors can be modelled using Coulomb friction only.
- the reel radii and inertias may considered to be constant in each operating point

Using Newton's law we can now derive the following set of differential equations:

$$\begin{aligned}
J_1\ddot{\varphi}_1 &= F_{s1}R_1 + \tau_{m1} && (4.9)\\
J_{m1}\ddot{\varphi}_{m1} &= K_{m1}I_{m1} - \tau_{m1} - \tau_{F1} && (4.10)\\
J_c\ddot{\varphi}_c &= R_c(F_{s2} - F_{s1}) && (4.11)\\
J_2\ddot{\varphi}_2 &= F_{s2}R_2 + \tau_{m2} && (4.12)\\
J_{m2}\ddot{\varphi}_{m2} &= K_{m2}I_{m2} - \tau_{m2} - \tau_{F2} && (4.13)
\end{aligned}$$

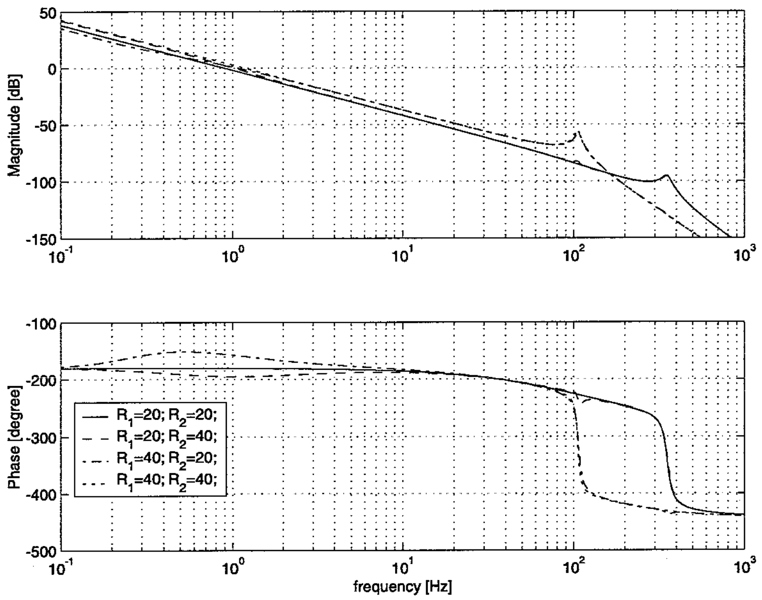

Figure 4.3: FRF of I_{m1} to φ_c at 4 reel radii combinations

with

$$\begin{aligned}
\tau_{m1} &= c_{m1}(\varphi_{m1} - \varphi_1) + k_{m1}(\dot{\varphi}_{m1} - \dot{\varphi}_1) && (4.14)\\
\tau_{m2} &= c_{m2}(\varphi_{m2} - \varphi_2) + k_{m2}(\dot{\varphi}_{m2} - \dot{\varphi}_2) && (4.15)\\
F_{s1} &= c_1(\varphi_c R_c - \varphi_1 R_1) + k_1(\dot{\varphi}_c R_c - \dot{\varphi}_1 R_1) && (4.16)\\
F_{s2} &= c_2(-\varphi_c R_c - \varphi_2 R_2) + k_2(-\dot{\varphi}_c R_c - \dot{\varphi}_2 R_2) && (4.17)
\end{aligned}$$

To design the controller, we need the input-output relation from I_{m1} to φ_c and I_{m2} to φ_c. Because the system is symmetric, the transfer functions of both I/O relations are similar, only opposite in sign (if the capstan rotates in positive direction, reel 1 also rotates in positive direction, but reel 2 rotates in negative direction). The relation is dependent on the radius of the reel, so we show the transfer function (figure 4.3) at 4 different reel radii combinations. A difficulty is that at this stage not all the model parameters are known, so we use estimates. The motor shaft parameters are provided by the motor supplier. The esimates for the paper damping and stiffness are obtained from [1]. When a prototype is build, it is possible to identify the parameters to get more accurate values. This identification procedure is described in chapter 8.1. The parameters used are listed in appendix A.

The systems with $R_1 = 20$ [mm] show an eigenfrequency at $f = 250$ [Hz], which is introduced by the motor shaft and coupling. As the radius of reel 1 becomes larger, this eigenfrequency shifts to $f = 100$ [Hz]. When designing a controller, this frequency shift can affect the closed loop stability, so it has to be taken into account. The change in radius of reel 2 has minimum effect on this transfer function, because of the relative high damping of the paper. Also the eigenfrequency at $f = 1$ [Hz], introduced by the paper dynamics, is strongly damped. For low frequencies we can see a small phase shift due to this eigenfrequency.

In the next chapter a stabilizing controller will be designed. In chapter 6 this model, including the controller and sensors, will be simulated using Matlab Simulink, to check whether implementation would work in practise.

Chapter 5

Controller design

The task of the controller is to keep a constant tension force in the paper and to control the translation of the paper. Figure 5.1 shows a block scheme which describes the control system. The tension force control will be implemented as a feedforward controller, which uses off-line estimation of the reel radii to set the torques on both DC motors. This part will be described in section 5.1. The position control is a feedback system which uses capstan position measurements to control translation of the paper. Friction compensation will be implemented to reduce the steady-state error. The design and stability analysis of this system will be described in section 5.2.

5.1 Tension force controller

The tension force controller uses the estimation of the reel radii to calculate the torque needed to keep the paper stretched with a certain tension force. As described in chapter 4, the range of one operation of the Image Verification Unit is limited to 0.2 [m] in tape length. In this range the reel radii can be considered constant. The torque needed for the tension force can then be expressed as a linear function of the radius

$$T_t = F_t R_1 \tag{5.1}$$

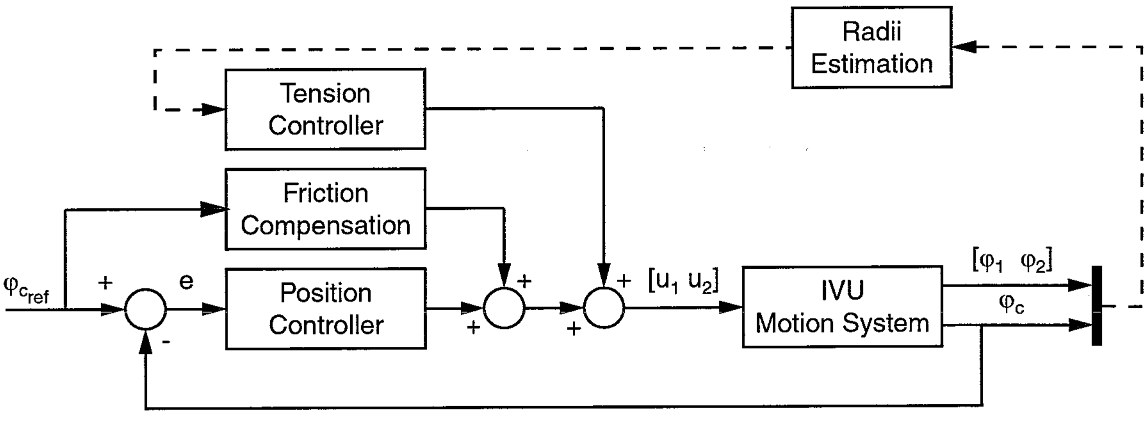

Figure 5.1: Block scheme of controller design

Thus during one operation the required torque can also assumed to be constant. It is then possible to estimated the reel radii off-line and implement the tension controller as a constant feedforward signal. The advantage here is that the controller is kept simple. We do not need an adaptive controller, which would increase the implementation costs. The controller will also not affect stability.

The value of the required tension force can be obtained from the torque delivered by the slip couplings at the current system. This torque is set to the value needed at the average reel radii and is equal to $T_t = 3.0 \cdot 10^{-3}$ [Nm]. At $R_{mean} = 30$ [mm] this gives $F_t = 1.0 \cdot 10^{-1}$ [N]. Because the capstan has a constant known radius, the reel radii can be estimated from the measured reel and capstan rotation by

$$R_1 = \frac{R_c \varphi_c}{\varphi_1} \tag{5.2}$$

When the rotation can be measured exactly, we only need a very small step to be able to give an precise estimation of the reel radius. However, because the measurements of all 3 rotation are quantized, we need a larger step to guarantee a certain accuracy of estimation. We can describe this accuracy as the relative influence of the quantization interval on the total rotation. This can be expressed as

$$accuracy = \frac{2\pi/increments}{rotation} \cdot 100 \quad [\%] \tag{5.3}$$

If we want to obtain an accuracy of 5% at the rotation of reel 1, we have to rotate $\varphi_1 = \frac{2\pi/209}{5\%} = 0.6$ [rad]. The maximum tape translation needed for this rotation is at maximum reel radius, hence the required paper displacement $x = \varphi_1 R_{1_{max}} = 24$ [mm] or $\varphi_c = 1.9$ [rad]. If we use an encoder with 500 ppr to measure φ_c, the accuracy of the measurement will be $\frac{2\pi/500}{1.9} \cdot 100 = 0.7$ [%]. The total accuracy is more than required as will be shown in the simulations in section 6.3.

5.2 Position controller

A requirement for designing the controller is to keep it as simple as possible in order to minimize the implementation costs. Of course, the controller also has to be robust, in this case this means that it has to be stabilizing for the complete range of reel radii. Other disturbances are not incorporated here. Because the system with $R_1 = 40$ [mm] the eigenfrequency introduced by the motor shaft is at the lowest frequency and of the highest amplitude, we expect this system to have the most critical stability margins. However, if we keep the closed loop bandwidth far below this eigenfrequency, we do not expect any influence of this eigenfrequency on the stability.

To develop the controller we will approximate the process as single mass for low frequencies ($f < 20$ [Hz]). The process transfer function can be written as $H_p = K_p/s^2$. To be able to place all the poles and zeros of the closed loop system, we need a PD-controller. With the controller transfer function $H_c = G(\tau_d s + 1)$, we can write the closed loop transfer function as:

$$H_{cl} = \frac{K(\tau_d s + 1)}{s^2 + K\tau_d s + K} = \frac{\omega_n^2(\frac{2\zeta}{\omega_n}s + 1)}{s^2 + 2\zeta\omega_n s + \omega_n^2} \tag{5.4}$$

where $K = GK_p$. The parameters will now be tuned by choosing frequency domain performance of the closed loop system.

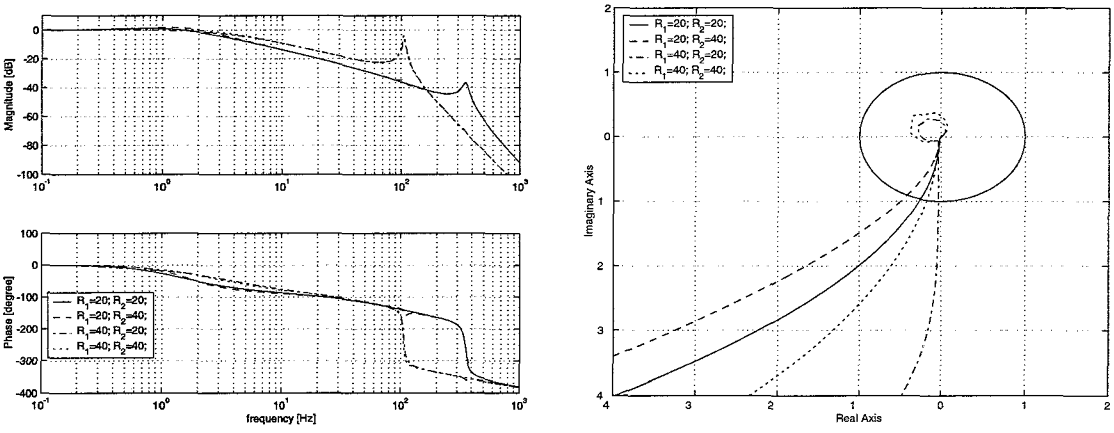

(a) *Closed loop transfer functions*

(b) *Nyquist plot of open loop transfer function*

Figure 5.2: Controller design plots

A problem with the IVU system is that it is not possible for the controller to inverse the direction by using one motor, because then the paper gets folded. When the change of direction occurs, the control should be taken over by the other motor. This switching system can be considered as a piece-wise linear system. If we find a stabilizing controller for both regions separate, we can say that the system is globally stable. To overcome this switching problem, it is desired to have an overdamped system, which has no overshoot at a step-response. For a system without a zero we can say that the system is overdamped as $\zeta > 1$. However, if a zero is present and this zero is close to the poles, it introduces extra overshoot. In the real system, friction introduces extra damping which is not incorporated in the controller design, so overshoot is then reduced. Therefor we choose $\zeta = 1$. For closed loop performance demands we do not need to have a high bandwidth. To be sure to stay within stability margins we choose a bandwidth of $\omega_n = 2\pi$ [rad/s]. Now we have two real poles at -2π [rad/s] and a zero at $-\pi$ [rad/s]. Although both poles are real, because the zero is dominant to the poles, we expect an overshoot in the step response of the simulation model. In the real system, where Coulomb friction is present, this overshoot will be reduced due to this friction. For the controller parameters we can now write $G = \omega_n^2/K_p$ and $\tau_d = 2\zeta/\omega_n$. With $K_p = 31.6$ we have $G = 1.25$ and $\tau_d = 0.32$.

If we now use this controller at the system as shown in figure 4.3, we obtain a robust and stable closed loop system for all reel radii. The bandwidth of the system for the complete range of reel radii is obtained from the closed loop transfer function, figure 5.2(a), at 0 [dB] cross-point. It varies from 1 to 2 [Hz], depending on the reel radii. The phase margin is obtained from the open loop Nyquist plot, figure 5.2(b), and varies from 75 [deg] for the system with $R_1 = 20$ [mm] and $R_2 = 40$ [mm] to 88 [deg] for the system with $R_1 = 40$ [mm] and $R_2 = 20$ [mm]. Further tuning will be done when the controller is implemented at the prototype, see chapter 8.2.

The friction acts as a disturbance on the steady-state error, so to further reduce this error we will compensate this friction. The friction force is modelled as Coulomb friction only. To decide in which direction the friction force acts, we need the direction of rotation of the reels. In order to keep the controller as simple as possible, we implement the friction compensation as a feedforward controller and will use the desired direction of rotation $\dot{\varphi}_{C_{ref}}$, hence

$$\tau_F = \tau_C \, sign\left(\dot{\varphi}_{C_{ref}}\right) \tag{5.5}$$

Chapter 6

Simulation

Before building and testing a prototype, it is important to know whether it is possible to implement the concept. This can be verified by making a simulation model which also incorporates the non-linear processes such as the encoders. The model derived in chapter 4 is implemented in Matlab Simulink. This chapter describes the simulation model and results, with and without a controller.

6.1 The process Simulink model

The main model (figure B.1) describes the equations (4.9) to (4.13). We choose the motor currents I_{m1} and I_{m2} as inputs, because these are the variables that can be controlled. The angular rotations φ_1, φ_2 and φ_c are chosen as outputs, because these are the parameters that can be measured. To check whether the model behaves as expected, a simulation is performed.

Figure 6.1 shows a simulation at $R_1 = R_2 = 30 \cdot 10^{-3}$ [m]. First both motor currents are set to a positive value, $I_m = 4.9 \cdot 10^{-2}$ [A], which is equal to the desired tension force at this radius. We expect the reels to rotate in positive direction, and due to paper stiffness come to an end deflection of $\varphi_i = \frac{I_{m_i} K_{m_i}}{c_i R_i^2} = 6.8 \cdot 10^{-2}$ [rad]. This is shown in figure 6.1(c). By increasing I_{m2} for 1 second, we expect the system to accelerate and then maintain a constant velocity. If we then increase I_{m1}, the system will decelerate. This is shown in figure 6.1(d). The tension force, shown in figure 6.1(b), increases during acceleration, but remains at the desired level during constant velocity.

At the prototype the rotations of both reels are measured by optical sensors which count 209 increments per revolution. These sensors can not detect the direction of rotation. To obtain a good simulation model, we will extend the main model with a model of these sensors. The implementation in Simulink is shown in figure B.2. The pulses given by these optical sensors are counted by a counter, which is shown in figure B.3.

The capstan rotation is measured with a rotational encoder. This device generates A & B pulses, which can be used for rotation and direction detection. We only have to quantize this rotation to get the measurement φ_c. In simulations we use an encoder with 500 increments per revolution.

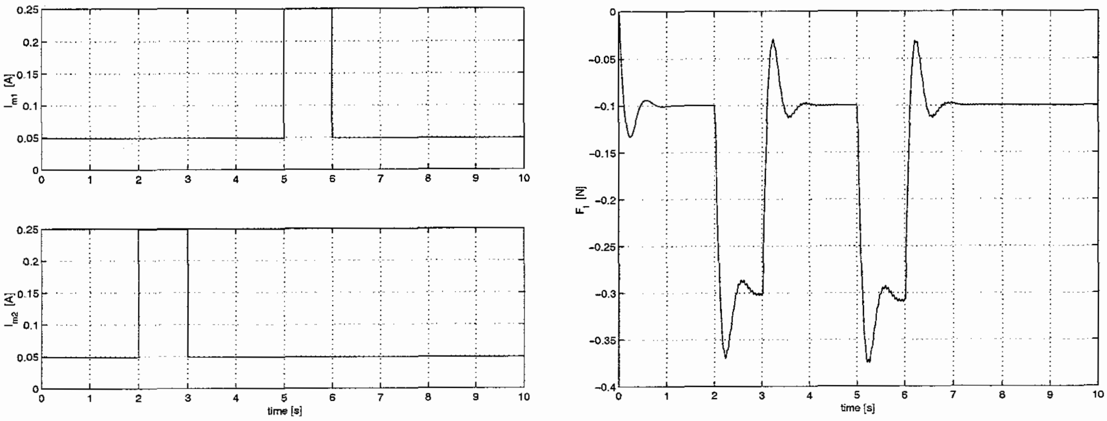

(a) Motor currents

(b) Tension force

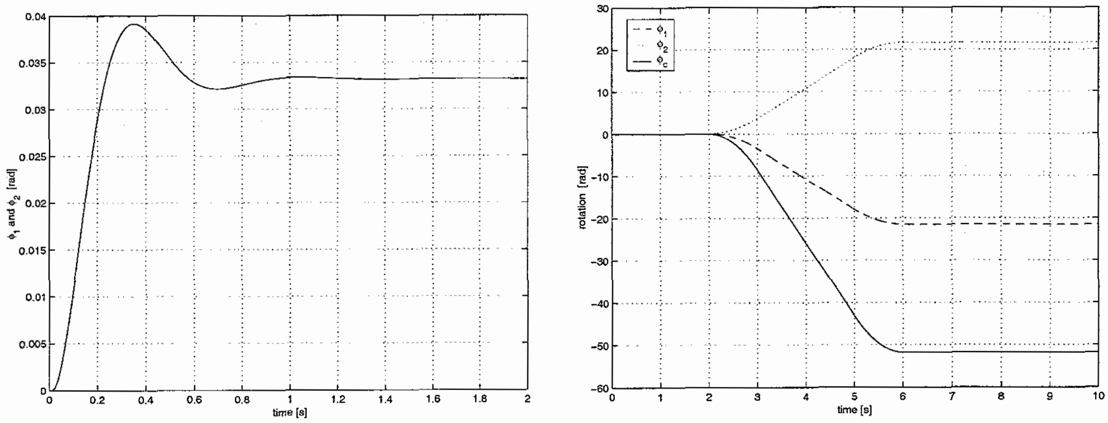

(c) Reel rotations for $t < 2$ sec.

(d) Reel and capstan rotations

Figure 6.1: Simulation at $R_1 = R_2 = 30 \cdot 10^{-3}$ [m]

6.2 Reel radii estimation

The reel radii are estimated using the known capstan radius and the reel and capstan rotation, as described in chapter 5.1, equation (5.2). When implementing this, we must be sure that the rotation is not reversed, because the optical sensor will only count upwards. The estimation will then not be accurate. In Simulink this is realized by setting a positive torque at motor 2 to put the system in motion, and we will use motor 1 to keep the paper under tension. Because the reel radii are not known in advance, we will use the minimum torques required. The tension torque is thus the torque needed when reel 1 is at minimum radius, the stepping torque is the torque needed to overcome the static friction level when reel 2 is at maximum radius. If the capstan rotation passes the required 1.9 [rad], the system is triggered and the reel radii are estimated and passed to the controller. The Simulink scheme is presented in figure B.4.

6.3 Controller implementation

To check whether the controller will behave as expected, we have implemented it at the extended Simulink model. The complete scheme is shown in figure B.5. Figure 6.2 shows the response of the system at $R_1 = 20$ [mm] and $R_2 = 40$ [mm]. We see that the closed loop behavior is stable and the system is overdamped. The overshoot, which would be introduced by the zero, is reduced by the Coulomb friction. The tension force is kept at the desired level during constant velocity. All reel radii combination show the same behavior. From these simulations we can conclude that it is possible to implement this system configuration, and obtain good results using a simple controller. A prototype can now be build and tested. The next chapters describe the implementation and test results of this system.

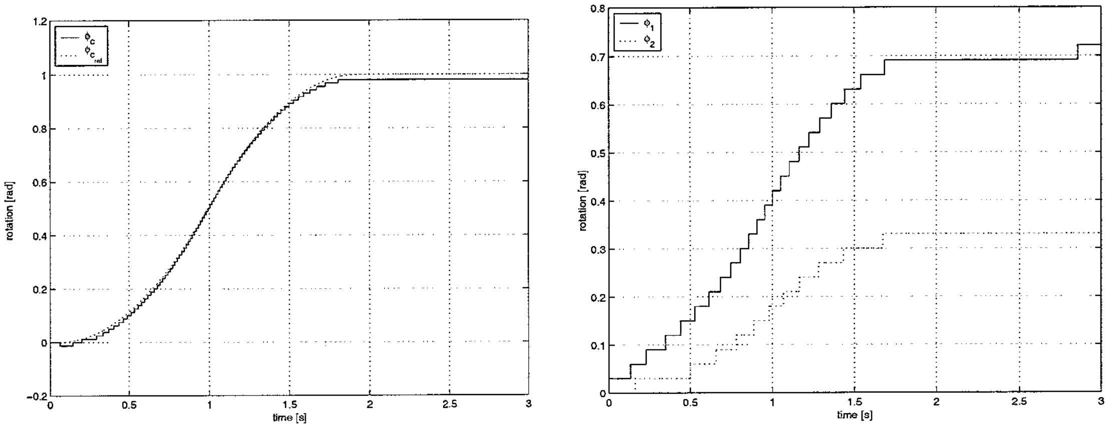

(a) Capstan rotation

(b) Reel rotations

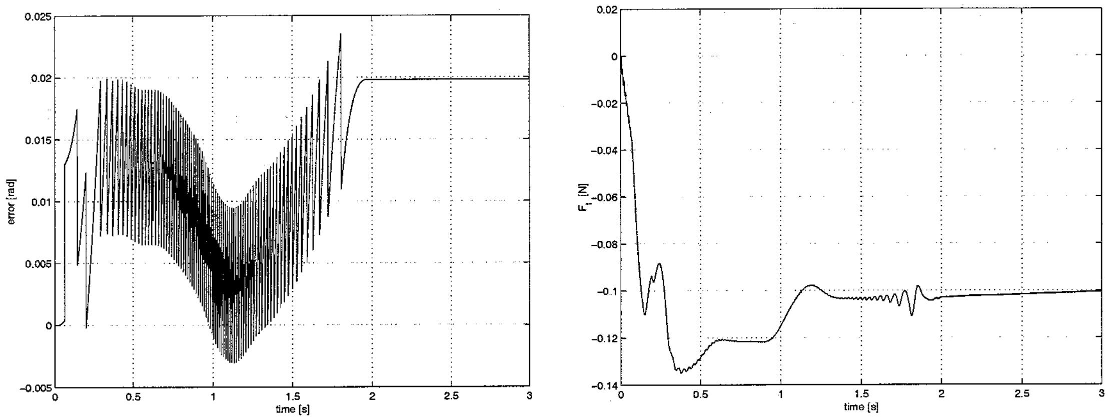

(c) Tracking error

(d) Tension force

Figure 6.2: Closed loop step response

Chapter 7

Practical setup

This chapter describes the test setup of the Image Verification Unit redesign. It consists of a data acquisition system which can be used from within Matlab and runs in real-time, two switch-mode drivers to drive the DC motors, two Iron Core DC motors, a quadrature encoder and two optical sensors.

7.1 Data acquisition system

For testing a system it is important to be able to continually measure and control it. To do this, we need a data acquisition system which is capable of measuring analog signals and digital signals (for encoder usage), but can also send out analog or digital controller signals. To be able to predict and control the timing behavior of a dynamical system, the data acquisition requires real-time performance. This section describes the implementation of "soft" real-time measurement and control using the AT-MIO-16-DE data acquisition board with Matlab Simulink, the Real Time Workshop and Wintarget. An overview of the complete system is shown in figure 7.1.

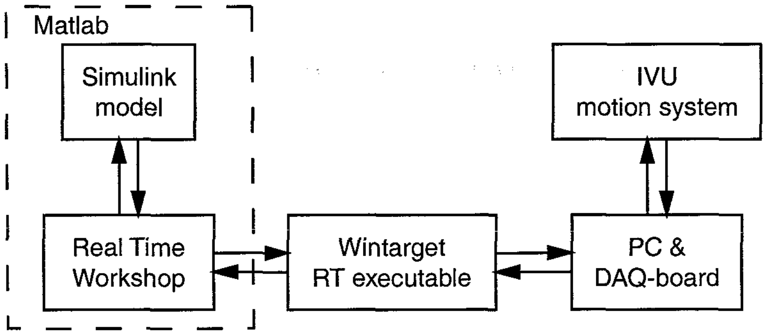

Figure 7.1: Schematic overview of the practical setup

7.1.1 Data Acquisition Card

The AT-MIO-16-DE multifunction I/O board from National Instruments features 12-bit ADCs with 16 analog inputs, 12-bit DACs with two voltage outputs, 32 lines of TTL-compatible digital I/O, and two 24-bit counter/timers for timing I/O.

Analog Inputs

The analog input can be set to measure referenced or non-referenced single inputs and differential inputs in uni- or bipolar mode with a voltage gain varying from 0.5 to 100 [-]. Unipolar input means that the input voltage range is between 0 and V_{ref}, where V_{ref} is a positive reference voltage of 10 [V]. Bipolar input means that the input voltage range is between $-V_{ref}/2$ and $+V_{ref}/2$. At the IVU motion system, the only analog signals that have to be measured are the optical sensor signals, which are voltages between 0 and 5 [V]. It is also possible to enable dithering. Dither, or additive white noise, has the effect of forcing quantization noise to become a zero-mean random variable rather than a deterministic function of the input signal. When you enable dither, you add approximately 0.5 LSB rms of white Gaussian noise to the signal to be converted by the ADC. This addition is useful for applications involving averaging to increase the resolution of the DAQ board as in spectral analysis. Because for the sensor measurement we only need to detect low or high logic level, dithering is not enabled. Another board function is multiple-scanning. With multiple-channel scanning you can increase the scanning speed and sample several signals as nearly simultaneously as possible. The maximum multiple-channel scanning acquisition rate is identical to the single-channel acquisition rate for all gains, which is 500 [kS/s]. The settling time of $T_s = 5$ [μs] is not increased as long as the gain is constant. When scanning among channels at various gains, the settling times may increase. We will use this multiple-scanning, so the scanning time will not limit the sampling frequency.

Analog Outputs

The analog outputs can be configured for either unipolar or bipolar output. A unipolar configuration has a range of 0 to V_{ref} at the analog output. A bipolar configuration has a range of $-V_{ref}$ to $+V_{ref}$ at the analog output. V_{ref} is an internal reference of +10 [V] or an external reference between -11 [V] and +11 [V]. The settling time of both output channels is 3 [μs]. The output voltages can not be set simultaneously. In the test setup, we will use both analog output channels to set the reference voltage of the motor drivers. Because the motors have to deliver torque in both direction, we shall use the analog output channels in bipolar mode.

Counter/Timers

The two 24-bit up/down counter/timers are available for a wide variety of timing and counting applications. Its up/down counting feature is particularly convenient for encoders. When using quadrature encoders with the DAQ-STC, you have two choices. First, for simple applications, you can connect the encoder directly to the DAQ-STC, without any extra logic or

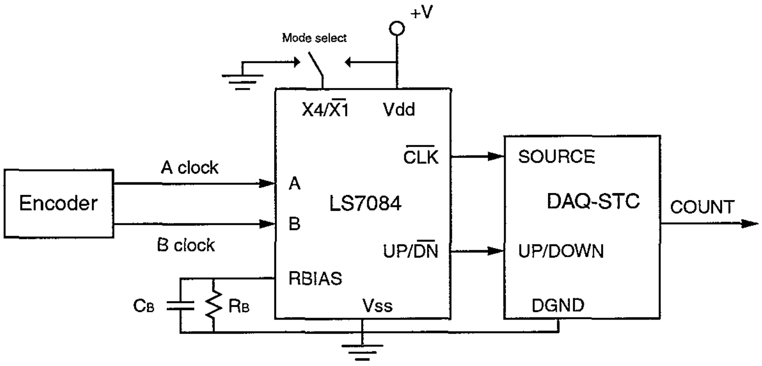

Figure 7.2: Encoder to counter interface using the LS7084

signal conditioning. Although simple to implement, this configuration has the disadvantage of not being able to discern between stationary vibration of the encoder and real rotation. Second, you can interface the encoder to the DAQ-STC using a using a quadrature clock converter IC. This method prevents errors due to jitter and debouncing, and provides higher measurement resolution. For control purposes we will implement the second method using the LS7084 quadrature clock converter from LSI Computer Systems. This IC converts the A and B signals from an encoder into a clock and up/down signal that you can connect directly to the DAQ-STC. The LS7084 includes lowpass filters to prevent miscounts due to noise and jitter. In addition, the LS7804 uses dual one-shots to prevent the miscounting produced by vibration, or dither. This interface is shown in figure 7.2.

7.1.2 Matlab and real-time

Using the Real-Time toolbox and the lcc-compiler it is possible to compile and run c-code created from your Simulink model. If this code is generated using the Wintarget template make file, a real-time executable is made. On execution, Wintarget installs an interrupt service routine that executes the code at the right times. The sample rates can vary from 1 [Hz] to what the pc is capable of.

Using this configuration it is also possible to add custom c-code to the Simulink model. In this way a device driver is created that handles communication between the real-time program and the DAQ card. In Simulink, this driver is presented as a masked S-function block. The user can read analog inputs and encoder values from, and write analog outputs to the AT-MIO-16DE-10 block. All the card function described in section 7.1.1 can be set by the user. In appendix D a detailed description of this block is given together with all the files and steps needed to create a real-time executable.

A problem occurred when trying to compile the generated code, because the DAQ card requires `double` and `unsigned long` variables. If this block code is not generated first, the variables are not declared at the beginning of a function. In c-code, this results in an error. This problem can be evaded by making sure that the driver block gets the highest priority. When the script `rtbuild.m` is used for building, all the blocks in the Simulink scheme are set to priority 1, but the driver block is set to priority -1.

Wintarget shows missed sample hits in an indicator. Real-time performance can be guaranteed when no samples are missed. Using a PIII based pc at 400 [Mhz] processor, a sample frequency of 800 [Hz] can be guaranteed if no other tasks are running. In the measurements we will set the sample time to $T_s = \frac{1}{500} = 0.002$ [s].

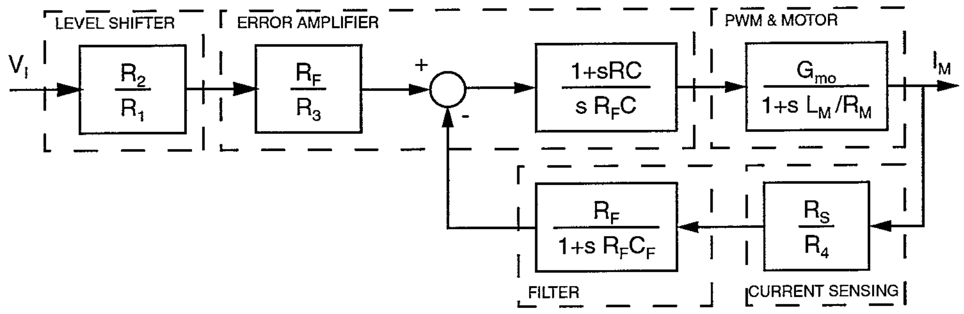

Figure 7.3: Block scheme of the L292 motor driver

7.2 DC motor driver

To control the power delivered by the motors, we need a motor driver which linearly transfers the analog voltage output of the data acquisition board into a current to the motor. We use the L292 Switch-Mode Driver from SGS-Thomson to perform this task. This is a pulse width modulation (PWM) type full-bridge driver and is capable of delivering 2 [A] current at 24 [V] with a maximum switching frequency of 30 [kHz]. The L292 consists of a level shifter, an error amplifier, a current sensing amplifier, a filter and a PWM. A block scheme is presented in figure 7.3. The electrical scheme of the motor driver with all its external components is given in appendix C. The transfer function from the reference input voltage V_I to the output current I_M can be written as:

$$\frac{I_M(s)}{V_I(s)} = \frac{R_2R_4}{R_1R_3}G_{mo}\frac{\frac{1+sRC}{1+sL_M/R_M}\left(1+sR_FC_F\right)}{\frac{1+sRC}{1+sL_M/R_M}G_{mo}R_S + sR_4C + s^2R_FR_4C_FC} \tag{7.1}$$

where $G_{mo} = \frac{1}{R_M}\frac{2V_S}{V_R}$, R_1, R_2, R_3 and R_4 are internal resistors, V_R is the internal reference voltage, V_S is the supply voltage, L_M is the motor inductance and R_M is the motor resistance. All the other variables can be chosen to meet the optimal conditions.

If we look at the DC transfer function ($s = 0$), we can calculate the sensing resistance value from

$$R_S = \frac{V_I}{I_M}\frac{R_2R_4}{R_1R_3} \tag{7.2}$$

At the maximum voltage output of the DAQ, $V_I = 10$ [V], the motor current must be at its maximum value, $I_M = 2$ [A], hence $R_S = 0.24$ [Ω]. In order to be sure that the closed loop system is stable, we first cancel the pole introduced by the PWM & motor by choosing:

$$1 + sRC = 1 + s\frac{L_M}{R_M} \tag{7.3}$$

Equation 7.1 is now reduced to a second order system with cutoff frequency and damping ratio

$$f_0 = \sqrt{\frac{G_{mo}R_S}{R_FR_4C_FC}}$$

$$\zeta = \sqrt{\frac{R_4C}{4R_FC_FG_{mo}R_S}}$$

If we now choose a damping ratio of $\zeta = \frac{1}{2}\sqrt{2}$, we get $C = 1.24 \cdot 10^{-4}R_FC_F$ [F]. If we look at the filter, we see that it has a cutoff frequency of $f = \frac{1}{2\pi R_FC_F}$ [Hz]. A recommended value

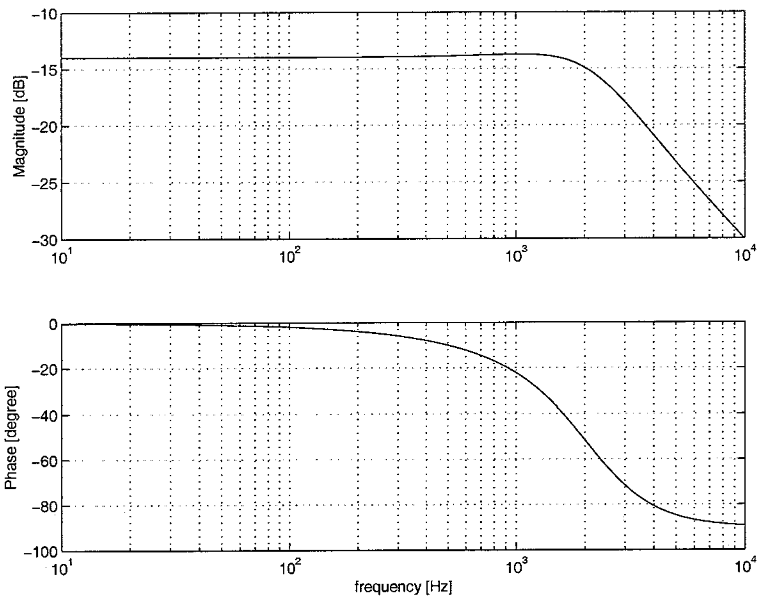

Figure 7.4: FRF of the L292 motor driver

for this bandwidth is 3 [kHz], hence $R_F C_F = 5.3 \cdot 10^{-5}$ [s] and $C = 6.6$ [nF]. From (7.4) we now have $R = 170$ [kΩ]. If we now choose $R_F = 510$ [Ω], we obtain $C_F = 104$ [nF]. The Bode plot of the transfer function is shown in figure 7.4. We can see that the bandwidth is larger than 10^3 [Hz], so the motor driver will not affect the performance of the IVU motion system. Because the L292 is a PWM motor driver, also the switching frequency must be set. This has no effect on the closed loop system, but only make the output stage more efficient. The frequency can be expressed as $f_{osc} = \frac{1}{2R_O C_O}$ [Hz] and will be set to 22 [kHz] using $R_O = 15$ [kΩ] and $C_O = 1.5$ [nF].

7.3 DC motors

In theory DC motors of any size are able to put the system in motion, but due to the tension and friction forces, these motors need to supply a torque from at least the maximum friction and the maximum tension torque to put the system in motion. We have performed some experiments to measure the friction torque. We placed a paper roll with maximum diameter at one reel and measured the current needed to put the reel in motion, thus to overcome the friction torque. From this measurement, together with the motor constant we can calculate the torque needed: $T_F = I_m K_m = 0.1 \cdot 61 \cdot 10^{-3} = 6.1 \cdot 10^{-2}$ [Nm].

For the required tension torque we use the torque applied by the slip couplings, which is $2.5 \cdot 10^{-3}$ [Nm]. The total minimum required torque is then $T = 6.4 \cdot 10^{-2}$ [Nm]. The motors used at the old system have a maximum torque of $2.5 \cdot 10^{-2}$ [Nm], so it is not possible to use these as direct drive DC motors. For simulation and testing the new concept we use an DC motor with a continuous torque of 0.45 [Nm], which is more than sufficient. For the motor specification see appendix E, motor `9904 120 53 707`.

7.4 Encoder and sensors

The controller developed in chapter 5 consists of a tension force control loop and a position control loop. Both controllers use position measurements to calculate the required torques. For the position control loop we need to measure the position of the paper. It is however not possible to measure this directly. By measuring the rotation of a capstan with known diameter, it is possible to get an estimation of the tape translation. To achieve an accurate estimation, we must be sure that no slip occurs between the paper and the capstan. It is possible to use the capstan with pressure roll (see figure 2.1) for this purpose. The required positioning accuracy is $1 \cdot 10^{-3}$ [m]. Because the capstan radius is $12.5 \cdot 10^{-3}$ [m], the required accuracy for the capstan rotation is $1 \cdot 10^{-3}/12.5 \cdot 10^{-3}$ [rad]. Therefor we need an encoder with a minimum of $2\pi \cdot 12.5 = 80$ increments per revolution. If, in the future, the print image is changed, and therefor the accuracy should be increased, it is advisable to use an encoder more increments than required. For testing and measurements we use an quadrature encoder with 2500 pulses per revolution. This is a higher resolution than used in simulations, so we do not expect that it introduces stability problems.

For the tension force control, we need to identify the roll radii. In the current system optical sensors are present at both reels, which count 209 increments per revolution. The ratio between capstan rotation and rotation of the reel will give an estimate for its radius, hence no extra sensors are needed to identify the reel radii.

Chapter 8

Test results

This chapter first describes the verification and identification of the dynamical model. Then the controller parameters are calculated so optimal performance and stability can be guaranteed. Finally section 8.3 shows results of step responses.

8.1 Parameter identification

In chapter 4 we derived a model to describe the IVU motion system. With the practical setup we can verify the obtained model, identify the model parameters and tune the controller parameters described in chapter 5. This identification procedure will be described in this chapter.

It is not possible to directly measure the frequency response function of the input motor current I_M to the capstan rotation φ_c, because the motor current cannot be directly measured by the DAQ board. We identify the frequency response function H_p from the output voltage u set in Simulink, and the measured rotation φ_c, so it includes the transfer function of both the DAQ card and the motor driver. In the previous chapter has been shown that the DAQ has a gain of 0 [dB] with a bandwith much larger than the IVU bandwith, so it has no influence on the IVU motion system transfer function H_{ivu}. The motor driver transfer function is also known, and we can then extract these transfer functions to obtain H_{ivu}.

The frequency response function is obtained by measuring the sensitivity S. An advantage of this method is that the system is actuated in closed loop. We will measure the sensitivity by adding a band limited white noise w to the controller signal u_c (see figure 8.1). The sensitivity can then be obtained from

$$S(s) \; = \; \frac{W(s)+U_c(s)}{W(s)} = \frac{1}{1+H_p(s)C(s)} \tag{8.1}$$

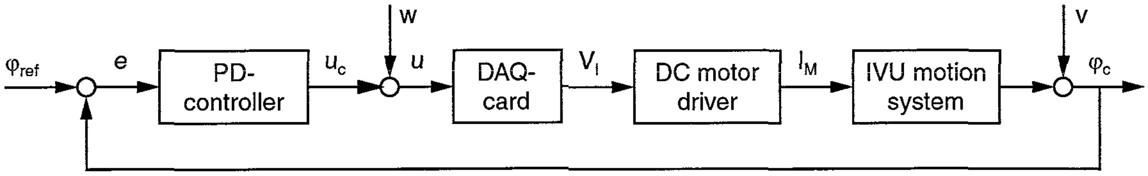

Figure 8.1: Sensitivity measurement

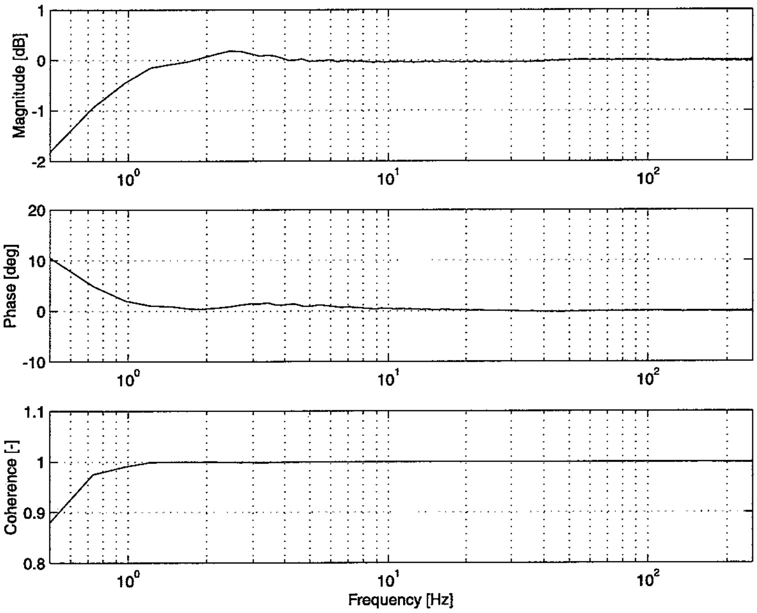

Figure 8.2: Sensitivity measurement

where H_p is the transfer function of the IVU motion system together with the DC motor drivers and the DAQ card, thus $H_p = \varphi_c(s)/u(s)$.

To reduce the influence of friction on the frequency response we use a constant velocity reference. The controller used during the measurement is a PD-controller with $P = 1$ [V/rad] and $D = 0.1$ [Vs/rad]. The system is excited with a random noise with a bandwidth up to 250 [Hz] with a RMS value so u is kept within ±5 [V]. The measured $S(s)$ is obtained by averaging 50 time series of 2048 samples at a sample frequency of 500 [Hz] with a Hanning window and 50% overlap. The measurements are performed at $R_1 = 38$ [mm] and $R_2 = 22$ [mm]. Figure 8.2 shows a bode plot of the sensitivity and the coherence of the measurement. We see that from $f = 1$ [Hz] the sensitivity $S \approx 0$ [dB] which indicates that the closed loop bandwidth is approximately 1 [Hz].

Now we can extract the controller and the motor driver from this measurement to obtain the process frequency response function H_{ivu}. To estimate the parameters, we try to fit the theoretical transfer function derived in chapter 4 on the measured FRF. Both the phase and magnitude are considered. Figure 8.3(a) shows both the measured and estimated FRF. We can see that the measurement data becomes very noisy from $f = 60$ [Hz], so these frequencies are not taken into account in the parameter estimation. The system shows a gain increase at $f = 2$ [Hz], which indicates mass decoupling of the second (not driven) reel. In the simulation model this decoupling occurred at $f = 1$ [Hz]. Hence, the paper stiffness c is higher in the real system. It also shows a damped eigenfrequency at $f = 40$ [Hz], which was at $f = 100$ [Hz] in the simulation but was less damped. Hence, the motor shaft stiffness c_m is lower and the motor shaft damping k_m is higher. Also the process gain shows to be lower, which indicates larger motor inertia J_m. At low frequencies, the phase of the real system turns towards 90 [deg], which means that friction is present in the system. At high frequencies, the measured FRF shows a larger phase delay than the estimated transfer function. Even at $f = 100$ [Hz] the phase still shows a decay. This is introduced by the time delay due to the sampling time $T_s = 0.002$ [s] and the zero order hold. The time delay in a system causes the original transfer function H_p to be multiplied by $H_d = e^{-j2\pi f\tau}$. It has constant amplitude $|H_d(f)| = 1$ and

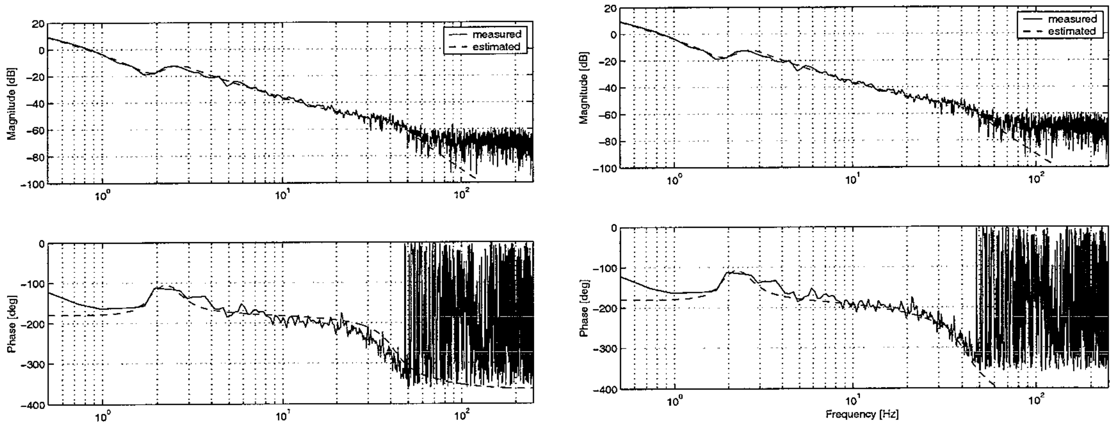

(a) Without time delay

(b) With time delay

Figure 8.3: Estimated and measured FRF

phase $\varphi_d(f) = -2\pi f \tau$. The total time delay τ can be expressed as

$$\tau \;=\; \frac{1}{2}T_s + T_c \tag{8.2}$$

where T_c is the time needed for calculations. In the test setup $T_c = T_s$, hence $\tau = 0.003$ [s]. Figure 8.3(b) shows the measured and estimated FRF with time delay. We can see that now also the phase is well estimated.

It is clear that the real system shows the same behavior as the dynamical model derived, and the PD controller described can also stabilize the real system.

For the feed-forward controller we need an estimation of the friction. Break-away and constant velocity experiments are performed to obtain measurements at different velocities. It is possible to estimate and compensate the friction using a Stribeck friction model as in equation (8.3), but the resulting controller would be complicated.

$$F_{Strib} \;=\; F_C + (F_S - F_C)e^{-(v/v_s)^2} + F_v v \tag{8.3}$$

As in chapter 5 is mentioned, it is preferred to undercompensate the friction, resulting in an overdamped system. For the friction compensation we take then the lowest measured Coulomb friction which results in a simple controller. The friction is estimated by measuring the voltage needed to keep the system at constant velocity, averaged over 12 capstan rotations. At $R = 37.5$ [mm] this equals 4 complete reel rotations. Figure 8.4 shows the results of friction measurements and estimation for reel 1. Reel 2 shows the same pattern, but estimation results in a slightly higher Coulomb part. The measured force in voltages is scaled by the motor constant and the motor driver DC gain to obtain the friction force in [Nm]. Because only φ_c can be measured accurately, and this rotation is used in feedback, the friction force is show as a function of $\dot{\varphi}_c$ and not of $\dot{\varphi}_1$.

The parameters obtained in both the identification and the friction estimation are listed in appendix A.

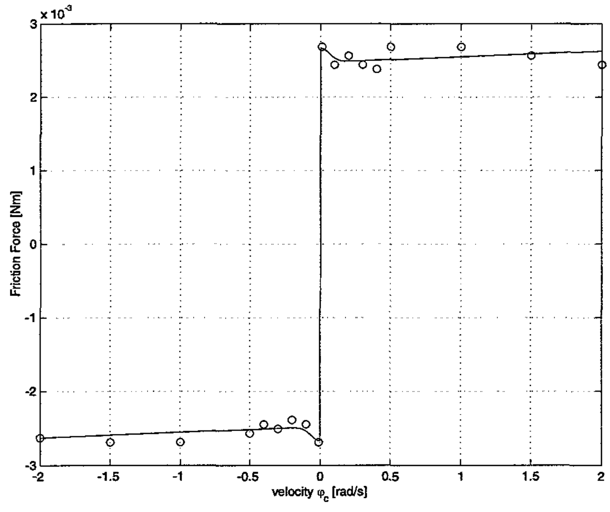

Figure 8.4: Friction measurement and Sribeck estimation

8.2 Controller implementation

Now we have identified all system parameters, we can tune the controller parameters using the procedure described in chapter 5. We first start with the feedback controller.
At $f = 1$ [Hz], the process gain $K_p = 25.4$. Because the eigenfrequencies introduced by the motor shaft are more damped, we can probably obtain a higher bandwidth without instability. Choosing a bandwidth of $\omega_n = 4\pi$ [rad/s] and damping $\zeta = 1$, we obtain $G = 6.2$ and $\tau_d = 0.16$ according to equation 5.4. Figure 8.5 shows the open and close loop responses, the sensitivity plot for both the measured and the estimated system (including time delay). The nyquist plot is only shown for the estimated system, because the measured open loop is too noisy at high frequencies, so the nyquist plot becomes unreadable.
We can see that the closed loop gain at low frequencies is lower in the real system, which is probably due to friction. The gain margin obtained is 6 [dB], the phase margin is 70 [deg], which means that the closed loop system is stable.
For the feedforward controller, we only need to set the friction force depending on the direction of rotation of the capstan. As shown in the previous section, the friction force shows a very small dependence on the velocity. Also the friction force has to be undercompensated to obtain an overdamped system. In the controller we will use the lowest friction force measured, i.e.:

$$T_F = 2.4 \cdot 10^{-3} sign\left(\dot{\varphi}_c\right) \tag{8.4}$$

8.3 Closed loop responses

To check wether the system behaves as expected, and is robust and stable for the complete range of reel radii, experiments are performed.
Figure 8.6(a) shows a step response with $R_1 = 25$ [mm] and $R_2 = 35$ [mm]. At $t = 0$ [s], the reference steps with -1 [rad]. Motor 2 is now used for position control and motor 1 is used for tension control. The resulting error is $e = 9.77 \cdot 10^{-3}$ [rad]. At $t = 3$ [s], the reference steps with $+1$ [rad]. The direction of rotation reverses, hence motor 1 is now used for position

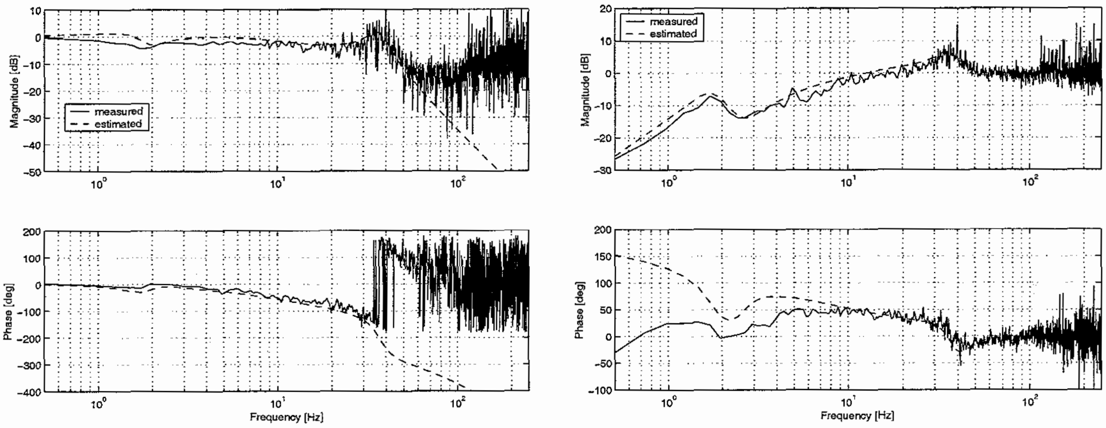

(a) Closed loop

(b) Sensitivity

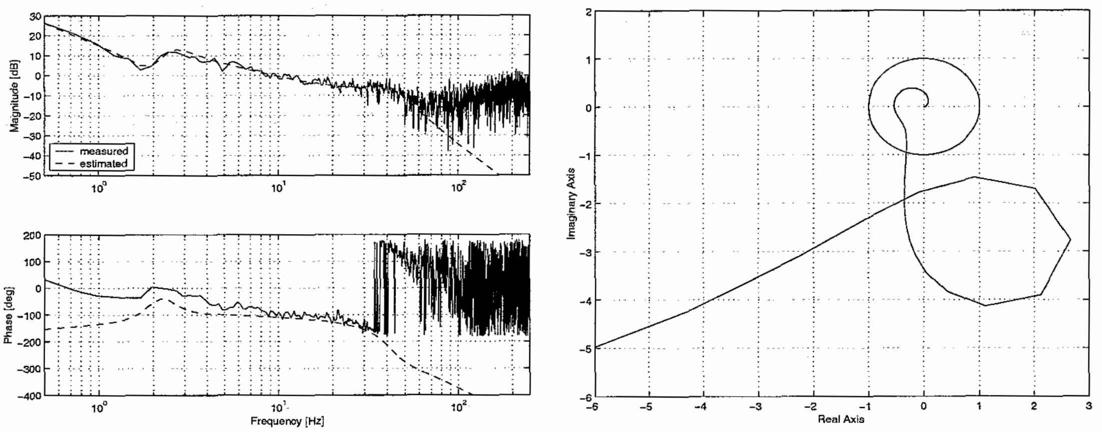

(c) Open loop

(d) Nyquist

Figure 8.5: FRF's for measured and estimated system

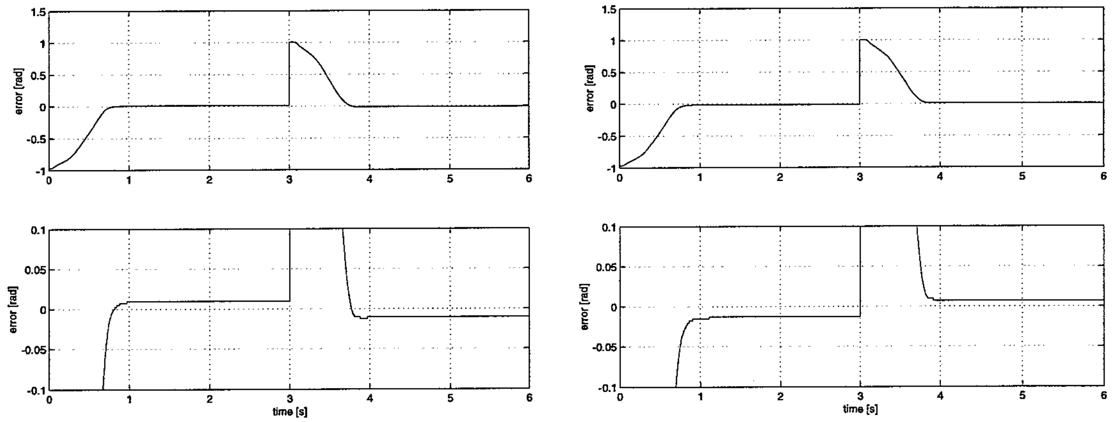

(a) $T_F = 2.4 \cdot 10^{-3}$ [Nm]

(b) $T_F = 1.5 \cdot 10^{-3}$ [Nm]

Figure 8.6: Closed loop step responses

control and motor 2 is used to set the tension torque. The resulting error is $e = -1.06 \cdot 10^{-2}$ [rad]. Both step responses show an overshoot. In chapter 5 we stated that it is desired to have an overdamped system to avoid direction switches. If we decrease the static friction compensation from $2.4 \cdot 10^{-3}$ to $1.5 \cdot 10^{-3}$ [Nm], as shown in figure 8.6(b), the step responses do not have an overshoot and the system is overdamped.

If the motor 1 is used to control the position (in both experiments the second step), figure 8.6(a) shows a larger overshoot and figure 8.6(b) shows a smaller steady state error. This indicates a higher closed loop gain, which is as we would expect because the radius of reel 1 is smaller than reel 2. We can see that the responses of both reel radii is stable and the resulting error is within the required margin, thus the closed loop system is robust.

In comparison to the old design, which had a positioning accuracy of ±1 [mm], the redesign improved the performance 10 times, resulting an accuracy of ±0.1 [mm].

Chapter 9

Conclusions and recommendations

In this part we have shown that it is possible to obtain good performance and robustness using simple control strategies and low-cost system parts. The redesign of the Image Verification Unit uses two DC motors to drive the reels both for positioning and keeping the paper under tension. This is significantly different from the old system, which uses two DC motors together with slip couplings to keep the paper under tension, and a stepper motor to position the paper.

Using a PD-controller, feedforward friction compensation and a feedforward tension controller, the positioning error of the paper in front of the CCD-camera is reduced 10 times in comparison to the present Image Verification Unit. The closed loop system is stable for the complete range of reel radii, and the position accuracy lies within the camera margin. However, we have seen that if the reel used for positioning has larger radius, the steady state error is also larger. This is because the loop gain is smaller at higher radius. Using gain scheduling, where the controller gain depends on the reel radius, the error can be further reduced. If higher performance is necessary, a more advanced controller can be developed and implemented.

Now it has been shown that the concept is practicable, the next step is to build a fully functional prototype. Attention must be payed to the implementation of the controller. It might be possible to implement it digital on the IVU pc, or on a separate micro-controller.
It is also recommended to use other DC motors. The DC motors used have a plastic transmission, and are therefor not highly durable. This transmission also introduces large friction forces, which increases the steady state error. Brushless DC motors are able to deliver the same continuous torque using a smaller transmission ratio.
The resolution of the encoder should be chosen according to the desired positioning accuracy. Simulations have shown that a resolution of 500 increments per revolution is accurate enough.

It is difficult to value the cost reduction, because the cost specification of the old design is not known at Stork Digital Imaging. We can only say that the costs decrease because the slip couplings and the stepper motor are eliminated, but increase because a quadrature encoder has to be used and the electronics (motor driver and controller) must be adjusted. By building the fully functional prototype more insight is obtained of the specific costs.

Part II

Analysis of the Linear Drive Unit

Chapter 10

Introduction

At the AX-series proofers, problems arise when printing a grey-image. The color spectrum of this print shows large deviation and a periodic pattern in this error ΔE. The main disturbance is a ± 19 [mm] pattern, which can be reduced to the performance of the Positioning Unit. This unit, shown in figure 10.1, consists of a Drum Unit and a Linear Drive Unit (LDU). The substrate used for printing is positioned on the drum. The task of the Drum Unit is to maintain a constant rotational speed during printing and to position the drum so the substrate can be handled. The task of the Linear Drive Unit is to position the print cassettes in front of the drum. It steps during printing with a step size of 1/12 or 1/24 [mm], depending on the print resolution. This translation is obtained by rotating a friction wheel (capstan) which is pressed against a steel strip. The position of the print cassettes is estimated by measuring the rotation of the capstan. Process disturbances, like variations in the capstan radius, cause the estimated position to differ from the real position. Here we see a direct relation between the ± 19 [mm] patterns in the color spectrum and the LDU, the capstan circumference is namely 18.8 [mm].

In this research first the relation between the position error and the color spectrum error of the grey image will be analyzed. Chapter 11 describes the origin of measurement errors and proposes three alternatives to reduce the effect of these errors on the image quality. With a view to increasing printer productivity, where the speed of positioning must be increased without loosing accuracy, the performance of the Linear Drive Unit will be analyzed in chapter 12. A few methods to optimize frequency response behavior are proposed.

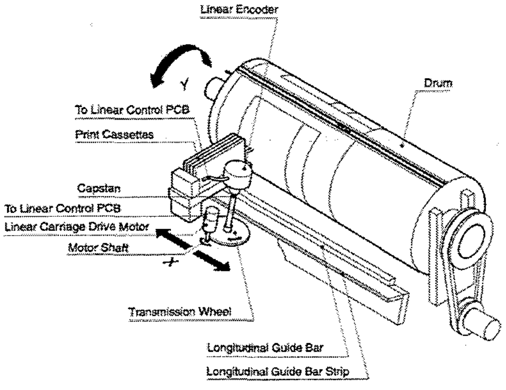

Figure 10.1: Linear Drive Unit

Chapter 11

Measurement Error

To realize the translation of the Linear Drive Unit, the capstan is rolls over a guide bar strip (see figure 11.1). The translation can be expressed as a linear relation between the capstan radius R_c and rotation θ_c, i.e.

$$x = R_c \theta_c \qquad (11.1)$$

To obtain the position for use in a control loop, the rotation of the capstan is measured by an encoder. The position is estimated by

$$\hat{x} = \hat{R}_c \theta_m \qquad (11.2)$$

where θ_m is the measured rotation. When using such an indirect measurement, care must be taken to the errors introduced by the estimation. All positioning errors introduce a deviation in the color, thus influence the image quality. The errors can be classified into two categories, random and systematic errors. The human eye is not sensitive to a small random error in the color spectrum of an image, so these errors do not directly influence the image quality. Systematic errors show a repeatable pattern. If this pattern is constant, it does not influence the image quality. However, if this pattern shows a (non-constant) periodic behavior, it has a direct effect on the image quality. The errors introduced due to mechanical inaccuracy in this system can be divided into these two classes. In section 11.1 we will give a description of the possible causes. Section 11.2 describes the relation between these errors and the color spectrum of an image. Finally we will propose some methods to reduce the error (section 11.3).

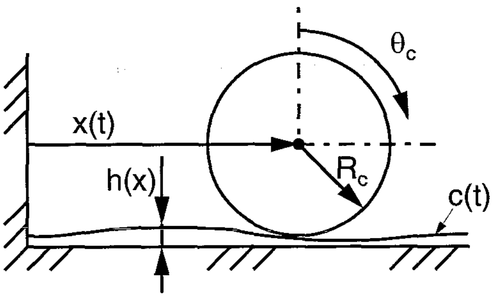

Figure 11.1: Capstan rotation over a guide bar strip

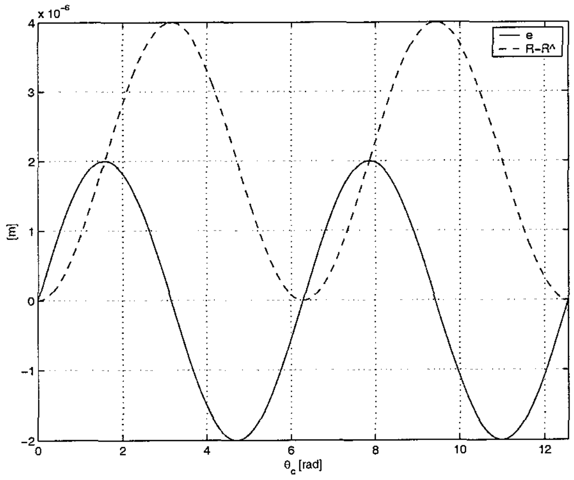

Figure 11.2: Capstan radius deviation and error

11.1 Origin of errors

Varying capstan radius

As we can see from equation (11.2), the position is a linear relation between the capstan radius and the capstan rotation. Due to production inaccuracy, the real capstan radius R_c differs in all probability from the expected radius $\hat{R}_c$. The radius can be written as a function of the rotation, i.e. $R_c = R_c(\theta_c)$. Because in the position estimation we use a constant capstan radius, the error $e_c = x - \hat{x}$ introduced by this estimation when the capstan rotates from θ_0 to θ_1 is

$$e_c = \int_{\theta_0}^{\theta_1} \left(R_c(\theta_c) - \hat{R}_c \right) d\theta_c \qquad (11.3)$$

which is thus also a function of the capstan rotation. As for any object, if the capstan rotates 2π [rad], it is in the same position again. Hence, we can write $R_c(\theta_c) = R_c(\theta_c + 2\pi)$. If the mean capstan radius $\bar{R}_c$ is equal to the expected capstan radius $\hat{R}_c$, we can see that over a rotation of 2π [rad], the integral (11.3) is zero. Hence, an error in the capstan radius introduces a periodic pattern with wavelength

$$\lambda_c = \int_0^{2\pi} R_c(\theta_c) d\theta_c \qquad (11.4)$$

This error can thus be classified as a systematic error. At the average expected capstan radius of $\hat{R}_c = 3$ [mm], we get $\lambda_c = 18.85$ [mm].

If the mean capstan radius $\bar{R}_c$ is not equal to the expected capstan radius $\hat{R}_c$, this will act as a constant in the integration. The error e_c shows also a linear trend.

Now lets say that the capstan is an oval with largest and smallest radii within the specification of $R_c = 3 \pm 0.002$ [mm], thus behaves as a sine wave over the rotation. The error introduced is than also a sine with amplitude 0.002 [mm], only shifted $\frac{1}{2}\pi$ [rad] due to the integration. This is illustrated in figure 11.2. The maximum error introduced depends on the initial condition $R_c(\theta_0)$. Here it is $e_c = 4 \cdot 10^{-3}$ [mm], which is more than allowed.

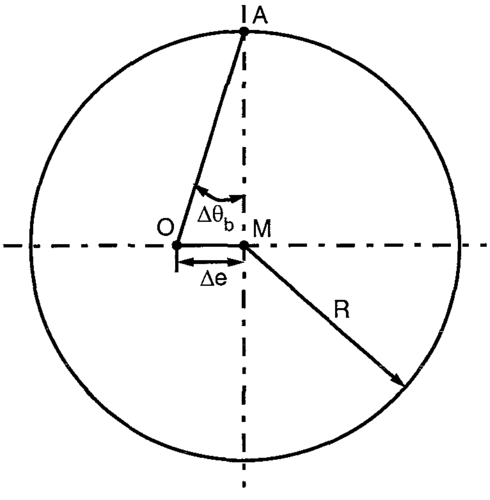

Figure 11.3: Measuring error caused by bearing eccentricity

Capstan bearings

If the capstan has an eccentricity to its bearings, or the bearings are not perfectly aligned, it causes the capstan to oscillate in the contact point with respect to its center. This can also be considered as a varying capstan radius, and the error it causes is described in equation (11.3).

Encoder bearing eccentricity

The encoder is provided with an integral bearing. Under normal circumstances, these bearing have an eccentricity to the graduation on the encoder disk. This causes a measuring error $\Delta\theta_b$ as shown in figure 11.3. Due to the eccentricity Δe, the encoder disk center M rotates around the center of the bearing O and translates thus also with regard to the scanning unit A. Only the translation perpendicular to line AM causes a measurement error. This translation can be expressed as a cosine of the rotation. Hence, the error is

$$\Delta\theta_b = \arctan\left(\frac{\Delta e_{max}\cos(\theta_e)}{R_g}\right) \tag{11.5}$$

From this expression we can see that the measurement error $\Delta\theta_b$ has a repeatable pattern with one full rotation as period. For the encoder used at the AX-series, with mean graduation radius $R_g = 19$ [mm], the maximum eccentricity of the bearing $\Delta e_{max} = 5$ [μm]. Hence, the error it causes is at the size of $\Delta\theta_b = 3 \cdot 10^{-4}$ [rad].

Encoder mounting eccentricity

The encoder is mounted using an externally mounted stator coupling. The purpose of this coupling is to provide an axial play, yet rotation stiffness, to catch the eccentricity in the capstan to encoder mounting. Every rotation of the encoder stator is a direct measurement

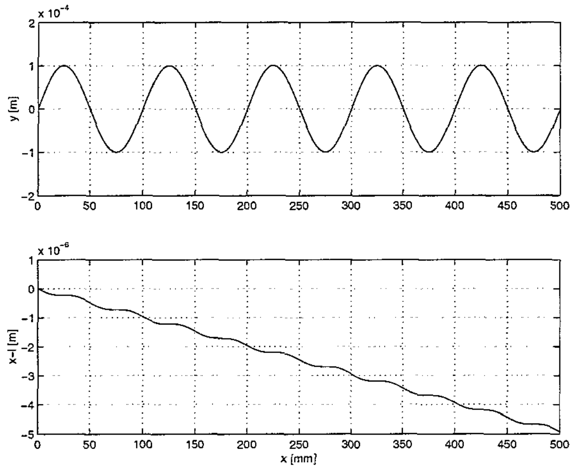

Figure 11.4: Position error due to varying guide bar strip thickness

error $\Delta\theta_m$. The coupling used is a variant on the Oldham coupling [6]. It has four sharp folded edges in a thin plate. This provides a good proportion between rotation and axial stiffness. It is however not completely rotational stiff due to an internal degree of freedom.
In the encoder to capstan mounting there exist an eccentricity due to the unroundness of the capstan bush. This eccentricity causes the encoder stator to displace axial, but probably also to rotate. Since the unroundness is repeatable every 2π radians, the obtained measurement error is a systematic error, and has the same effect on the measurement as the bearing eccentricity. It is difficult to quantify the size of the error, but even a minor rotation of $\Delta\theta_m = 10^{-3}$ [rad] causes a significant error in the position measurement of 3 [μm].

Guide bar strip thickness variation

The capstan is pressed against the guide bar strip to translate its rotation into a translation of the complete unit (see figure 11.1). The strip is placed against a extrusion profile which carries the complete unit. The guide bar strip can be seen as a path $c(t) = (x(t), y(t))$. The distance travelled by the capstan moving along this path is the integral of speed with respect to the time travelled, i.e. the path length is

$$l = \int_{t_0}^{t_1} ||c'(t)||dt = \int_{t_0}^{t_1} \sqrt{x'(t)^2 + y'(t)^2}dt \tag{11.6}$$

The physical meaning of variable $y(t)$ is the variation in the thickness of the steel strip from its nominal value, but it also incorporates the flatness of the extrusion profile. If this thickness is constant, $y(t) = 0$, we can see from equation (11.6) that the path length is equal to the position of the printheads, i.e. $l = x(t)$. However, if the thickness is not constant buy depends on the position x, and thus $y(t) = h(x(t)) - h_0$, we see that the path length is not equal to the position of the printheads, and the error introduced is $e_l = x - l$.
In all probability, the thickness of the steel strip is not constant. It might even be possible that due to the production process of the strip, the thickness varies at a repeatable wavelength. This is however not likely and the error on the position can therefor be seen as a random error.
To get an idea of the size of the error the varying thickness causes, figure 11.4 shows a simulation where y is a function of the position, i.e. $y(x) = 0.1\sin(\frac{2\pi}{100}x)$ [mm]. We see that even with this extremely large deviation, the resulting error is very small.

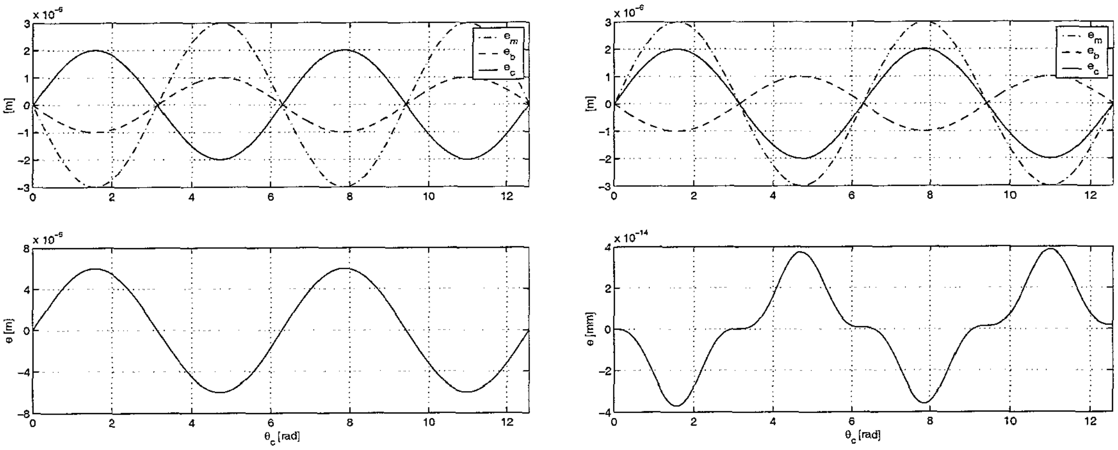

(a) Worst case

(b) Best case

Figure 11.5: Interaction of errors

Dirt

The Linear Drive Unit is very sensitive to dirt. Dirt at the guide bar strip result in a local deviation of the thickness h, thus has a direct effect on the position error. The dirt is randomly distributed over the strip, hence the error it causes is random. Dirt at the capstan results in a local deviation of the capstan radius R_c, and the error it causes is described in equation (11.3). If the dirt stays on the capstan during printing, it can cause a repeatable error with wavelength as in equation (11.4). This is however not likely, and we consider this error also as a random error.

Slip

The transmission between the capstan and the guide bar strip is based on friction forces. If the force actuated by the capstan exceeds the static friction level, slip between the capstan and the guide bar strip can occur. This slip is a relative motion of the two contact areas, this means that the real translation x is not equal to the expected translation $\hat{x}$. The slip causes thus a direct error $e_s = x - \hat{x}$. We assume the slip to occur randomly, hence the error it causes is also random. If the guide bar strip or capstan is polluted, the static friction level is reduced and slip is more easily to occur.

Interaction of errors

All the phenomena described above have an effect on the position of the printheads. It does not directly mean that all introduced errors fortify each other, they can also work against each other. The total error is a combination of the systematic and random errors.
From equation (11.2) we see that the expected translation is a linear combination between the expected capstan radius $\hat{R}_c$ and the measured rotation θ_m. This rotation can be expressed as

$$\theta_m = \theta_e + \Delta\theta_b + \Delta\theta_m \quad (11.7)$$

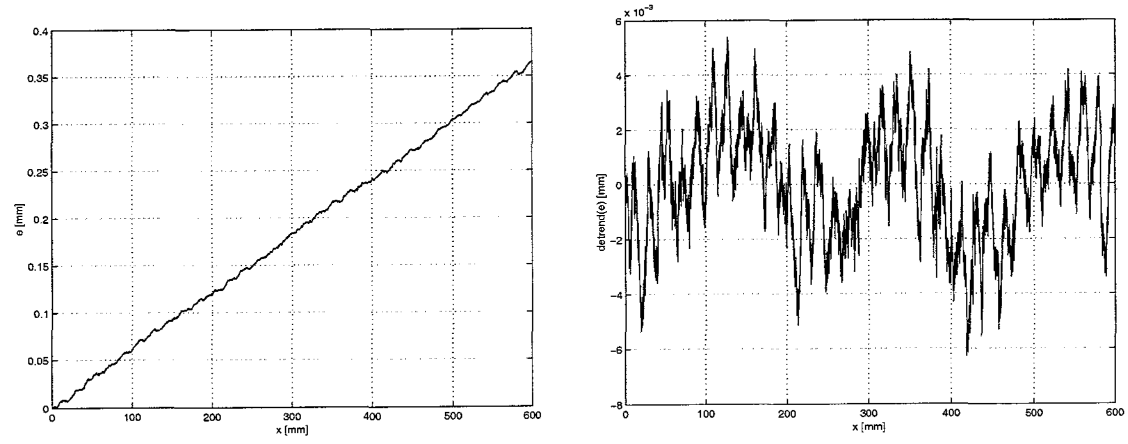

(a) With linear trend *(b) Without linear trend*

Figure 11.6: Position error e

Due to these measurement errors, we can rewrite equation (11.3) as

$$e_{sys} = \int_{\theta_0}^{\theta_1} R_c(\theta_c) d\theta_c - \int_{\theta_{m_0}}^{\theta_{m_1}} \hat{R}_c d\theta_m \tag{11.8}$$

This equation describes all the systematic errors in the system. Together with the guide bar strip error e_l and slip error e_s, the total error can be written as

$$e = e_{sys} + e_l + e_s \tag{11.9}$$

Here the errors due to dirt are not explicitly mentioned, because these can be reduced to e_c and e_l.

Now lets consider a scenario, where the random errors are zero and where the capstan is an oval as described before, the encoder bearing eccentricity is 5 [μm] and the error introduced by the stator coupling is a cosine with amplitude $\Delta\theta_m = 10^{-3}$ [rad]. Equation (11.8) describes the total error. In the worst case, the measurement errors are in phase and the capstan error is shifted π [rad] as shown in figure 11.5(a). The error e has now a maximum of 6 [μm]. The best case, where the mounting error is also shifted π [rad], the resulting error e is nihil. This is shown in figure 11.5(b).

11.2 Relation color spectrum and positioning error

To quantify the position error e as described in equation (11.9), we mounted a linear encoder at an AX-series proofer to obtain a direct measurement x_m of the printheads. The encoder used is a LIDA 477 system from Heidenhain with a resolution of 0.5 [μm]. If mounted according to the specification of Heidenhain, the absolute position accuracy of this system is ± 0.05 [μm] over 1 [m] measuring length.

We measured the error during printing of a grey image. The measurements are obtained at a sample rate of 500 [Hz]. To reduce the measurement noise, the data is filtered using a discrete second order Butterworth with a cut-off frequency of 50 [Hz]. Using **filtfilt** from Matlab, the data is filtered forward and reversed to get zero phase delay. Figure 11.6(a) shows

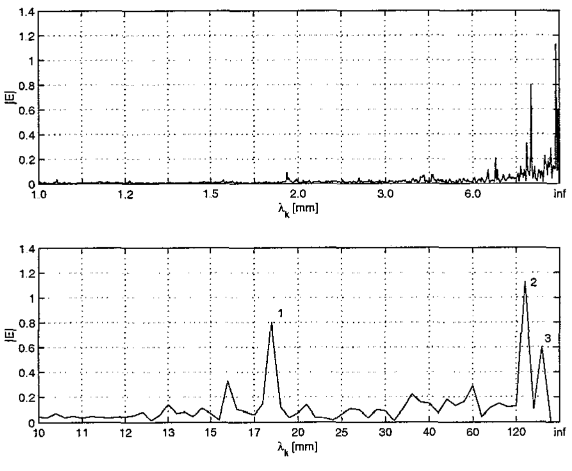

Figure 11.7: Fourier transform of the error

the measurement error e over 600 [mm]. It shows a large positive linear trend, which indicates that the capstan radius is larger than expected. Over 600 [mm], the error increased 0.36 [mm] due to this trend, so the deviation in capstan radius $\bar{R}_c - \hat{R}_c = 1.8$ [μm]. To highlight the periodic pattern in the error, we removed the linear trend as shown in figure 11.6(b). The wavelength of the error with respect to the **position** can be analyzed using a discrete Fourier analysis:

$$\begin{aligned} E(\lambda_k) &= \frac{1}{N}\sum_{n=0}^{N-1} e(n)e^{-j2\pi n\Delta x/\lambda_k} \qquad (11.10) \\ \text{with} \quad & \lambda_k = inf, x_e, \frac{x_e}{2}, ..., \frac{x_e}{N} \quad ; \quad N = \frac{x_e}{\Delta x} \end{aligned}$$

where E is the Fourier transform of the error, λ_k the wavelength, N is the number of measurement points, Δx is the distance between two measurements and x_e is the total measurement length. For the Discrete Fourier Transform holds $E(\lambda_{N/2+k}) = E(\lambda_{N/2-k})$, so the DFT can be seen as folded around the wavelength $\lambda_{fold} = \lambda_{N/2}$. Because we use a discrete Fourier analysis, we must take account for signal-leakage. If there are wavelengths in the signal of different size than the discrete λ_k values, the energy of these wavelengths leaks to the neighbouring wavelengths.

For this analysis, we use $N = 1200$, thus the shortest wavelength we can see is $\lambda_k = 1$ [mm]. To reduce the effect of signal-leakage we use a Hanning window. We also take the error without the linear trend, because this would only introduce more signal-leakage at long wavelengths. Figure 11.7 shows the amplitude $|E|$ as a function of λ_k on two different scales. We see three high peaks in the amplitude (bottom plot). The first one, at $\lambda_k = 18.75$ [mm], is clearly due to the combination of varying capstan and encoder eccentricities. The second and the third peaks, at $\lambda_k = 150$ [mm] and $\lambda_k = 300$ [mm], are most likely due to the guide bar strip thickness.

To produce the color grey, all CMYK[1] colors have to be used, and therefor a grey image is the most sensitive to system errors. When an image is printed, it is possible to measure its color spectrum L^*a^*b values[2] dependent on the position. A perfect image will show constant

---

[1] The four ink colors used for printing are Cyan, Magenta, Yellow and blacK (CMYK).

[2] This color model is based on the model proposed by the Commission Internationale d'Eclairage (CIE) in 1931 as an international standard for color measurement. In 1976, this model was refined and named CIE $L*a*b$. $L*a*b$ color is designed to be device-independent and perceptually uniform. $L*a*b$ color consists of a luminance or lightness component ($L*$) and two chromatic components: the $a*$ component (from green to red) and the $b*$ component (from blue to yellow).

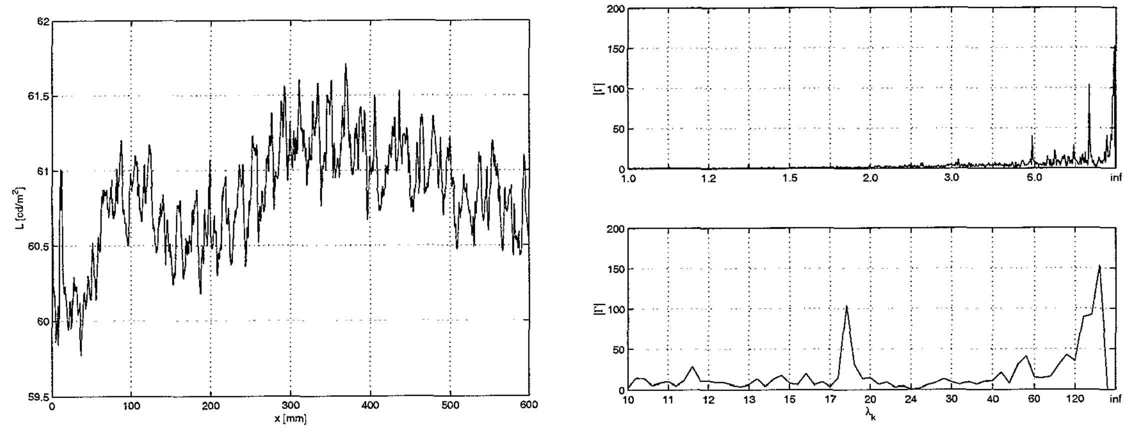

(a) Luminance of grey image

(b) Fourier transform of the Luminance

Figure 11.8: Grey-image color spectrum data

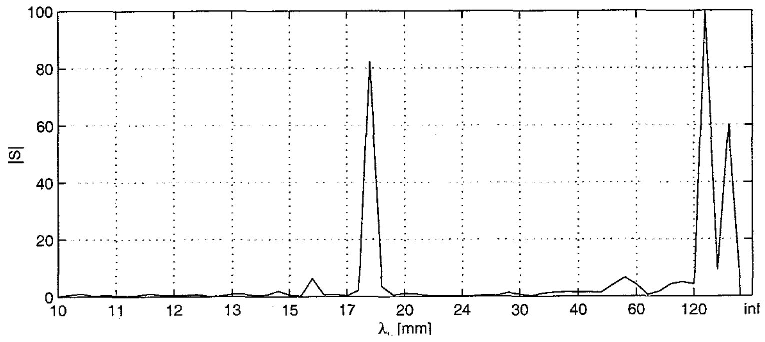

Figure 11.9: Cross power spectrum S

values. If we perform a Fourier analysis as in equation (11.10) of the measured luminance L with respect to the position, it is possible to obtain the wavelength of the error in [m]. We use Γ as the Fourier transform of the luminance L. Figure 11.8(a) shows the Luminance measurement. We show again the Fourier spectrum on two different scales in figure 11.8(b). The Fourier spectrum clearly shows high amplitudes at long wavelengths and a peak at $\lambda_k = 18.75$ [mm].

To search for the relation between the two signals, we calculate the cross power spectrum as $S(\lambda_k) = E(\lambda_k)\Gamma(\lambda_k)$. The result is shown in figure 11.9. This figure clearly shows the effect of the mechanical errors described in section 11.1 on the color spectrum deviation. To improve the grey-image consistency, the position errors have to be reduced or even eliminated.

11.3 Error reduction

As shown in the previous section, the difference in real position of the printheads and the expected position has great effect on the quality of an image. In practise, especially the ±19 [mm] wavelength cause the proofer to fail the quality demands of Stork Digital Imaging. It is therefor desirable to reduce these errors. This can be done in a few different ways.

The first method is to increase all specifications of the Linear Drive Unit. The maximum

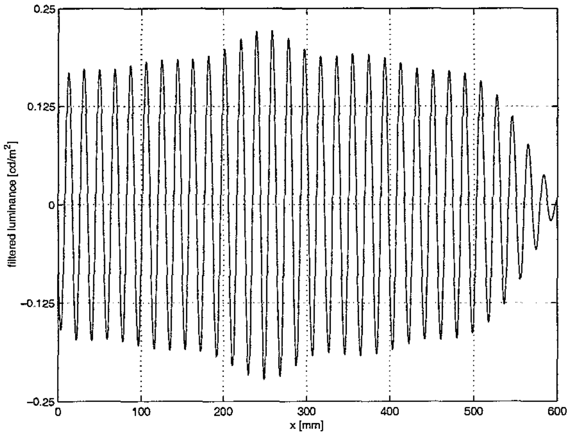

Figure 11.10: Filtered luminance

capstan radius deviation, the encoder mounting eccentricity and the guide bar thickness deviation (which incorporates the extrusion profile) should all be decreased. This is possible, however, the system costs would also increase with increasing accuracy. The random position errors introduced by dirt and slip would still be present in the system. Also due to wear of the system parts, the errors could increase when using the proofer.

A second method could be to use the spectrum data of a grey (or similar) image to calculate the expected position error introduced by the Linear Drive Unit. With this data, a correction of the expected translation (equation (11.2)) with respect to the expected error $\hat{e}$ could be made, i.e.

$$\hat{e} = f(L,\Gamma) \tag{11.11}$$

$$\hat{x} = \hat{R}_c\theta_m + \hat{e} \tag{11.12}$$

However, due to signal leakage of the Fourier transform, the wavelengths can not be determined at 100% certainty. For the wavelengths close to 18 or 19 [mm], we know that these are most likely introduced by the capstan and encoder errors. The real wavelength is then approximately as in equation (11.4). If this wavelength could be determined exactly, and the absolute rotation of the capstan and the shape and phase of the error with respect to this rotation are known, these errors could be reduced. If these conditions are not known within a certain margin, correction could lead to larger position error.

To get an absolute measure for the rotation of the capstan, an absolute angular encoder can be used, so this would not be a problem. The exact λ can also be determined rather straightforward, as it is exactly one full rotation of the encoder/capstan. If the luminance data is filtered using a band pass filter to obtain only the relevant wavelength, also the shape and phase of the error could be determined. Figure 11.10 shows the luminance filtered with a second order butterworth filter with frequency band $\frac{1}{20} \leq \omega_k \leq \frac{1}{17}$. The result is a relative constant amplitude wave with $\lambda \approx 18.75$ [mm], and we could find the relation $\hat{e} = f(L,\Gamma,\theta_m)$.

With this method, the errors introduced by the varying guide bar thickness, dirt and slip would still have effect on the image quality. The effect of wear of the capstan and encoder could be reduced by frequently measure the color spectrum deviation and determine the expected error.

A third method to reduce the position error is to use a direct measurement method. When measuring the absolute position of the printheads using a linear encoder, the phenomena as described in section 11.1 have no effect on the position error. The only measurement error left is the accuracy of the encoder.

This method has more advantages then only providing an accurate measurement. Using the current indirect measurement, increasing system time performance would be risky, as the probability slip occurs would also increase. Because slip has no effect on the position measurement using a direct measurement, it is more easy to obtain higher system performance. Also the requirements of the individual system parts of the Linear Drive Unit can be decreased, while maintaining the same position accuracy.

Currently, during the assembly process at Stork Digital Imaging, it takes much time to optimize the Linear Drive Unit so the proofer meets its quality demands. Also, many service calls for color deviation in the grey image come in, which cost a lot of money. Often, this color deviation is only due to dirt or wear of the system. Using the direct measurement method, both the assembly time and service calls can be reduced. Naturally, all methods described ask for an investment on one side, and give profits on the other side. It is left for further research to value all these profits and costs. The decision whether to optimize performance by changing the Linear Drive Unit, is not based on technical innovation only, but on this cost analysis.

With a view to increasing printer productivity, where the speed of positioning must be increased without loosing accuracy, the performance of the Linear Drive Unit will be in the next chapter. A few methods to optimize frequency response behavior are proposed.

Chapter 12

Performance

The performance of a system is defined by all the static and dynamic relations of that system. Without a model it is mostly difficult to predict how the performance will change when changing a system parameter. For example, if we want to increase the speed of positioning, it could be sufficient to use a stronger DC motor. It is however also possible that other factors are limiting the performance. Sometimes it is possible to derive a model by deduction from physical laws only, resulting in a white box model. However, if no prior knowledge is available, a model can be obtained from measurement, resulting in a black box model. The advantage of the black box approach is that the obtained model incorporates all the phenomena that have effect on the input-output relation. It is however difficult to reduce this relation to physical parameters, and it is not always possible to see the effect of a system parameter on the model. This is possible using the white box model.
To get insight in the physical relations of the Linear Drive Unit, and to be able to predict how to optimize the performance of the Linear Drive Unit, section 12.1 describes the modelling of the LDU mechanics using a white box approach. This model is verified by a black box identification in section 12.3, but first the electronic part of the LDU is described in section 12.2. Section 12.4 describes how to use the system parameters to increase the performance using the white box model. Section 12.5 describes the effect of the use of friction wheels as transmission on the performance of the LDU. Section 12.6 describes the identification of friction in the LDU. Finally, section 12.7 gives an analysis of the controlled used at the LDU, and how to optimize this.

12.1 Modelling

We define the system boundary as all rotating and translating parts, shown in figure 12.1. Here the motor, transmission wheel and encoder are modelled as rotating bodies with a certain inertia. The motor shaft is modelled as a rotational spring/damper with a rotating body at the end. The inertia of this body is negligible. The capstan is modelled as two rotational spring/dampers with a body with a certain inertia in the middle. The complete unit is modelled as a translating mass, which is connected rigid to the capstan. In this way we neglect the dynamics of the printheads and other accessories at the LDU. As input we define the motor current, i.e. $u = I_m$, and as output we define the absolute position $x = R_c\theta_c$ of the mass. The complete system state is defined by four rotations and their derivatives,

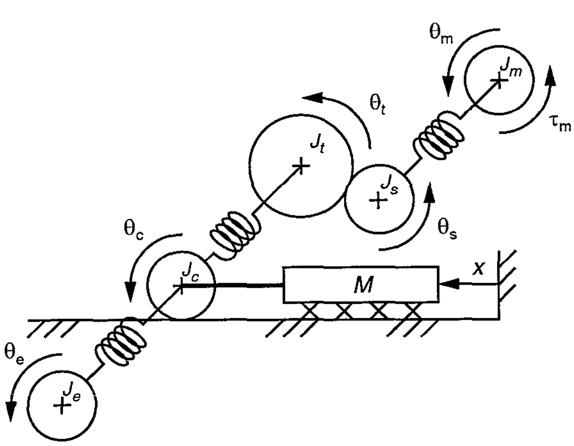

Figure 12.1: Representation of the Linear Drive Unit

i.e. as state vector we choose $\mathbf{x} = [\theta_m \;\; \dot{\theta}_m \;\; \theta_t \;\; \dot{\theta}_t \;\; \theta_c \;\; \dot{\theta}_c \;\; \theta_e \;\; \dot{\theta}_e]^T$. In state space this system can be written as:

$$\dot{\mathbf{x}} = A\mathbf{x} + Bu \tag{12.1}$$

$$y = C\mathbf{x} + Du \tag{12.2}$$

Where

$$A = \begin{bmatrix} 0 & 1 & 0 & 0 & 0 & 0 & 0 & 0 \\ -\frac{k_s}{J_m} & -\frac{b_s+K_{m2}}{J_m} & \frac{Nk_s}{J_m} & \frac{Nb_s}{J_m} & 0 & 0 & 0 & 0 \\ 0 & 0 & 0 & 1 & 0 & 0 & 0 & 0 \\ \frac{Nk_s}{J_t} & \frac{Nb_s}{J_t} & -\frac{k_c+N^2k_s}{J_t} & -\frac{b_c+N^2b_m}{J_t} & 0 & 0 & & \\ 0 & 0 & 0 & 0 & 0 & 1 & 0 & 0 \\ 0 & 0 & \frac{k_c}{J_c+MR_c^2} & \frac{b_c}{J_c+MR_c^2} & -\frac{2k_c}{J_c+MR_c^2} & -\frac{2b_c+B_c+R_c^2B_m}{J_c+MR_c^2} & \frac{k_c}{J_c+MR_c^2} & \frac{b_c}{J_c+MR_c^2} \\ 0 & 0 & 0 & 0 & 0 & 0 & 0 & 1 \\ 0 & 0 & 0 & 0 & \frac{k_c}{J_e} & \frac{b_c}{J_e} & -\frac{k_c}{J_e} & -\frac{b_c}{J_e} \end{bmatrix}$$

$$B = [\,0 \;\; \frac{K_{m1}}{J_m} \;\; 0 \;\; 0 \;\; 0 \;\; 0 \;\; 0 \;\; 0\,]^T$$

$$C = [\,0 \;\; 0 \;\; 0 \;\; 0 \;\; R_c \;\; 0 \;\; 0 \;\; 0\,]^T$$

$$D = 0$$

The complete derivation of the dynamical model is shown in appendix F. Figure 12.2 shows the input output relation of the system if the damping is neglected. To explain the location of resonances (pole-pair) and anti-resonances (zero-pair), we can divide the system in three inertia-spring-inertia subsystems. Of each subsystem we define the actuator as the inertia on which the input force acts. Such a system introduces a anti-resonance - resonance if the position of the actuator is measured, otherwise it introduces a resonance only. Every resonance gives a phase shift of -180 [deg], and every anti-resonance gives a phase shift of 180 [deg].

If we consider the capstan spring infinite stiff, the first subsystem is the motor-spring-capstan. Here the motor is the actuator and the position of the capstan is measured, thus this system introduces a resonance, at $f = 2.1 \cdot 10^3$ [Hz]. The second subsystem is the transmission wheel-spring-capstan. Here the transmission wheel is the actuator, and thus this system introduces also a resonance, here at $f = 114$ [Hz]. The third system is the capstan-spring-encoder. Now the position of the actuator, the capstan, is measured, hence this system introduces an anti-resonance at $f = 254$ [Hz] and a resonance at $f = 286$ [Hz]. After this frequency the phase delay is 360 [deg].

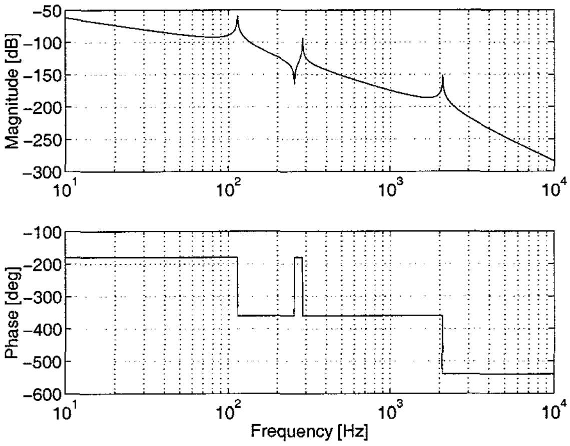

Figure 12.2: Bode plot

If we choose θ_e as output, we would have also seen three resonances, but no anti-resonances. The phase delay from $f = 286$ [Hz] is then 540 [deg]. This means that by measuring the position using a rotational encoder, we obtain a different input-output relation than by measuring the absolute position of the LDU.

12.2 Motor Driver

The motor driver scales the input voltage into a current and controls the current provided to the motor. The system used here is comparable to the one described in chapter 7, but uses two separate IC's. The direction or polarity of the output signal depends on a direction (logic) signal, thus for the reference input holds $V_i \geq 0$.

Because the torque provided by the motor depends linear on the current ($\tau_m = K_m I_m$), it is desired that the current is also a linear function of the input voltage. To find this relation, an experiment is performed.

To measure the current provided to the motor, a resistance of 1 [Ω] is connected between the motor and the electronics. The voltage over this resistance is a measure for this current since $V = IR$. During the experiment, the motor was fixed to obtain maximum load. Experiments are performed with both high frequency and static inputs. Up to 2 [kHz], the motor driver shows the same input-output behavior. For simplicity, here only the measurements with static input are described.

As input we provided a constant voltage ranging from 0 to 3 [V] with steps of 0.1 [V]. The measured current is averaged over 7500 samples. Figure 12.3 shows the results. We see that the relation between the input voltage and the output current is nonlinear. Below $V_i = 0.8$ [V], the current is $4.2 \cdot 10^{-2}$ [A], which is equal to $\tau_m = 8.8 \cdot 10^{-4}$ [Nm]. This means that without friction the system starts to move, which is undesired. We see later that the static friction level is higher than this minimum torque, so this is not a problem. However, if the static friction level is lower, it could cause instability of the controlled system. For $0.8 \leq V_i \leq 3.0$ [V], the relation could be approximated by a linear relation using the least squares method. Due to a zener diode, which is used to protect the current controller, input voltages higher than 3 [V] would result in a maximum current output. The current controller feedback voltage is cut off at this voltage, so at higher input voltages the error can not be corrected. As a result, the motor driver delivers maximum output current. In other words, the zener diode causes instability of the current controller when the input exceeds 3 [V]. The motor is only capable

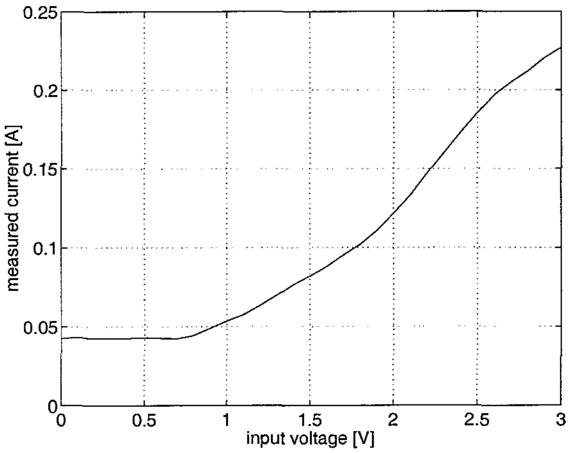

Figure 12.3: Motor driver input-output

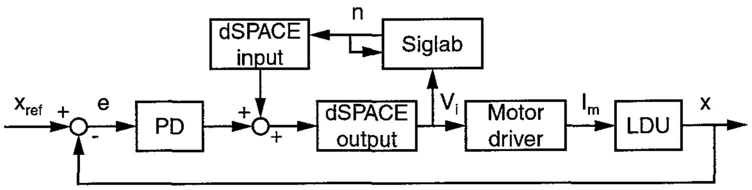

Figure 12.4: Experimental setup of Sensitivity measurement

of handling this current for a very short time, so $V_i > 3$ [V] should be avoided. At $V_i = 3.0$ [V], the maximum current of 0.23 [A] is thus reached, which corresponds to $\tau_m = 4.8 \cdot 10^{-3}$ [Nm]. This is less than 40 % of the maximum continuous torque of the motor.
The resulting input-output relation of the motor driver can be divided into three parts, hence

$$I_m = \begin{cases} 0.042 & \text{if } V_i < 0.8 \\ 0.042 + 0.1(V_i - 0.8) & \text{if } 0.8 \leq V_i \leq 3.0 \\ 5 & \text{if } V_i > 3.0 \end{cases} \tag{12.3}$$

12.3 Identification

We identify the Frequency Response Function (FRF) $H_{LDU}(j\omega)$ by measuring the sensitivity S in closed loop. The controller used is a PD-controller with $H_c = 1 \cdot 10^3(1 + 0.1s)$, obtaining a open loop bandwidth of 2 [Hz]. A random noise, with a bandwidth of 1000 [Hz], is added by the Siglab system. The sample frequency of the dSPACE system is set to 10 [kHz]. The experimental setup is shown in figure 12.4. To reduce the effects of friction, experiments are performed at constant velocity. Figure 12.5(a) shows the sensitivity measured at $\dot{x} = 5$ [mm s^{-1}] and noise RMS value of 0.25 [V]. In this way V_i is kept within the linear range of the motor driver. The FRF is estimated by averaging 50 time series of 8192 samples at a sample frequency of 2 [kHz]. Different measurements at noise RMS values varying from 0.05 [V] to 0.5 [V] show the same sensitivity. However, if V_i exceeds 3 [V], H_{LDU} is highly non-linear, and S is different each experiment.
Figure 12.5(b) shows the resulting LDU frequency response function from 1 to 250 [Hz]. From 50 to 220 [Hz] the FRF shows several damped resonances, which can not be directly reduced to the resonances found in the model. This is probably due to other features mounted at the

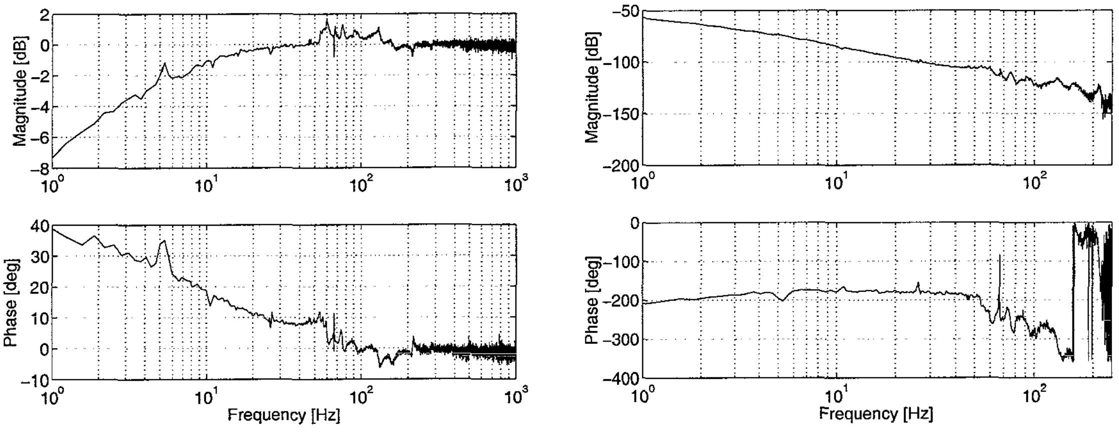

(a) Sensitivity measurement

(b) Resulting Frequency Response Function

Figure 12.5: Linear Drive Unit identification

LDU, like the printheads. To be able to reduce all the resonances to physical parameters, a modal analysis should be carried out. Up to 50 [Hz] the system behaves as a mass-damper system, with a gain similar to the derived model if scaled with $I_m = 0.1V_i$. The white box model is thus a good approximation at low frequencies. However, we will keep the high frequencies resonances in the model to describe the effect of changing system parameters to optimize input-output behavior, as described in the next section.

12.4 Input-Output optimization

If we want an optimal response of the system to the power delivered by the motor, it is desired to make the open loop gain as high as possible and shift the system resonances and anti-resonances to high frequencies. With increasing process gain also the open loop gain increases, and it is therefor desired to obtain a high process gain. These conditions depend on physical system parameters, hence it is possible to use these parameters to optimize performance. At the LDU, the parameters that are free to change are the radius of the capstan R_c, the radius of the transmission wheel R_t and partly the weight of the system M. We will use the white box model to find the optimal physical values. The resonances found by the black box model will be left out of consideration. The effect of the capstan radius on the gain and eigenfrequencies is shown in figure 12.6(a). We can see that with increasing R_c on the gain is not unambiguous. To decrease the total inertia of the system, thus to obtain a higher process gain, it is necessary to decrease R_c. However, with decreasing R_c also the force delivered by the capstan on the mass is decreased, and as a result also the process gain is decreased. If the capstan radius is increased, the stiffness k_c increases and thus the first two resonance and anti-resonance shift to the right in the Bode plot.
The effect of changing the transmission wheel radius is also not so straightforward. This is shown is figure 12.6(b). Reducing R_t will reduce the inertia J_t, but also reduce the transmission ratio N. This will both influence the process gain in the opposite. With decreasing inertia, the resonance at $f = 114$ [Hz] will shift to the right. Both these effects are shown in figure 12.6.
Reducing the mass M will always result in a higher process gain, but this effect is negligible.

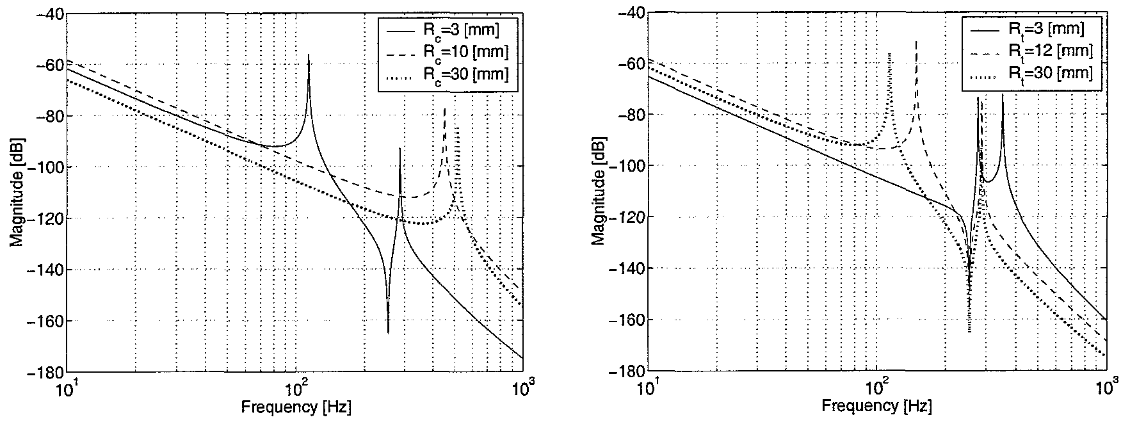

(a) *varying R_c, $R_t = 30$ [mm]*

(b) *varying R_t, $R_c = 3$ [mm]*

Figure 12.6: Effect of varying system parameters on input-output relation

The first two resonances will shift to the right when reducing the mass.

To obtain the optimal gain for this LDU model, the capstan radius should be increased to $R_c = 6.2 \cdot 10^{-3}$ [m] and the transmission wheel radius should be decreased to $R_t = 23 \cdot 10^{-3}$ [m]. The increase of the process gain at low frequencies is 4 [dB].

This optimization gives a first good approximation, however to find the optimal physical values at the real system black box identification measurements with different capstan and transmission reel radii should be carried out.

12.5 Friction wheel transmissions

The use of friction wheels (motor shaft, transmission wheel and capstan) put a large limitation on the maximum allowable motor torque. The contact force in these friction wheels is inversely proportional to the radii of these wheels. If this force exceeds the static friction level in these contacts, slip will occur. The static friction can be expressed as a linear relation between the normal force and a friction coefficient f, i.e. $F_s = fF_N$ [N]. For dry steel contacts $f = 0.8$, but due to dirt the value of f can significantly decrease, and slip is more easily to occur. The motor is pressed against the transmission wheel with a normal force of $F_N = 12$ [N], hence the maximal torque the motor can deliver before slip occurs is $\tau_{max} = 14$ [mNm], which is more than the maximum continuous torque the motor is capable of. The capstan is pressed against the guide bar strip with a normal force of $F_N = 20$ [N], thus the maximum torque the motor can deliver before the capstan starts to slip is $\tau_{max} = 2.5$ [mNm]. It is then desired to increase the wheel radii or to increase the normal force.

The most significant limitation on the performance is thus the transmission between the capstan and the guide bar strip. To optimize this, the first step is to increase the normal force to its maximal value, i.e. the value where no plastic deformation the guide bar strip, the capstan or the bearings occurs. If this should be no limitation, we can say that $F_N \geq \frac{\tau_m N}{R_c f}$ where τ_m is the maximum torque the motor is capable of. For the present design this means that $F_N \geq 125$ [N]. For the optimized system as described in section 12.4, the pressure force can be reduced to $F_N \geq 46$ [N].

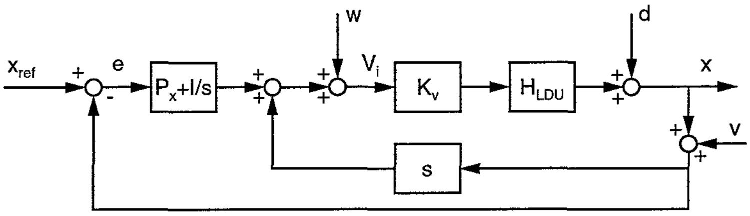

Figure 12.7: Linear Drive Unit controller

12.6 Friction

Friction is a combination of various phenomena, which all depend on the relative displacement and velocities between two surfaces. Normally, the friction is described by the Stribeck effect. This means that the friction force may decrease continually from the static friction level and increase with increasing velocity (equation (8.3)). However, near zero velocity and for small displacements the friction shows a nonlinear behavior, called stiction. Physically this phenomenon can be interpreted as two moving surfaces that are in contact by a large number of bristles with a certain stiffness. As a result, the system acts as a spring in this region. In high precision systems, this effect could cause significant limitation on the position accuracy.

In the Linear Drive Unit, the presliding behavior could be caused by the linear carriage. If the stiction phenomena is present, the frequency response function measured with excitation below the static friction level should result in a spring-mass system [7]. Experiments show that the Linear Drive Unit behaves as a normal mass system with small damping. This does not directly mean that the system does not show this behavior, but we can conclude that the sticking regime smaller than the encoder resolution. Since the static friction level depends on the normal force between two surfaces, the presliding regime is likely to increase with increasing weight of the Linear Drive Unit. This effect should thus be taken into account when changing the construction weight, for example at the Eagle 4 series.

To quantize the Stribeck effect, break-away and continuous velocity experiments are performed. The break-away experiments show a static friction level of $F_s = 0.93$ [V] for positive direction and $F_s = 0.88$ [V] for negative direction. This difference is probably caused by the flexible cable support, which acts as a very weak spring on the LDU. The constant velocity experiments do not show a decrease in friction force for small velocities, nor a significant viscous friction level. This can also be seen from the identified transfer function in figure 12.5(b). Viscous friction causes the slope of the transfer function to be -1 (or -90 [deg] phase delay) at low frequencies, which is not the case.

12.7 Controller

The task of the controller is to track a fixed reference path, resulting in a minimum positioning error. The first requirement to achieve this, is to obtain a stable closed loop system, i.e. all the poles of the closed loop transfer function must be placed in the left half plane. Because there are uncertainties in the Linear Drive Unit, such as varying capstan radius, we must make sure that the closed loop system is robust stable. To reduce the sensitivity of the plant to deviations in the process and input and output disturbances, it is desired to have a high open loop gain in the frequency band of interest. For fast tracking, it is desired to obtain

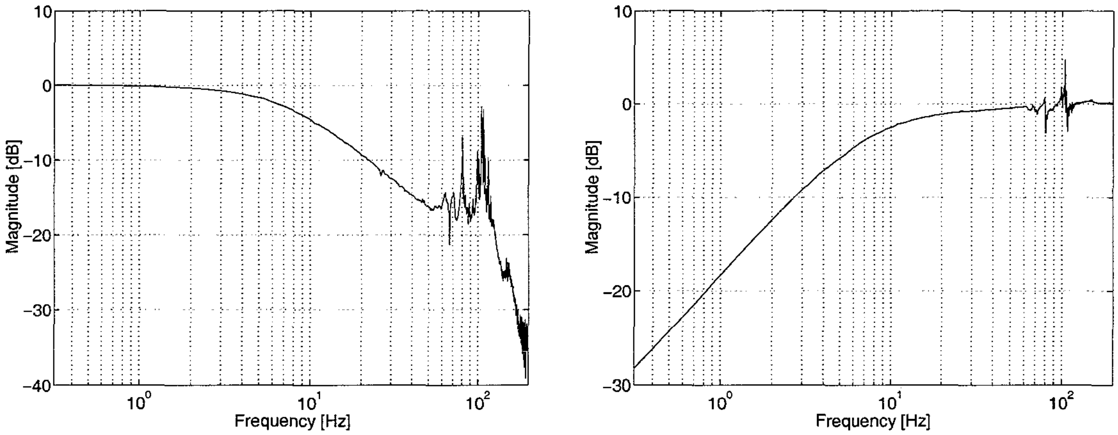

(a) Closed loop system

(b) Sensitivity

Figure 12.8: Transfer functions with present controller

a high closed loop bandwidth. However, in the presence of measurement noise, making the closed loop gain close to 1 also has the effect of transmitting the sensor noise directly to the output and the error. So the bandwidth should not be greater than necessary to meet specifications on set-point response and disturbance reduction. It is desired that the closed loop transfer function is rolled off outside the passband. Also, if the closed loop bandwidth exceeds the natural bandwidth of the process, the actuator may not be able to provide the required power.

The present controller of the Linear Drive Unit can be represented as in figure 12.7. Here is w the disturbance on the input, the process deviation like friction and varying capstan are represented by d and v is the measurement noise. The controller can be divided into two parts, a velocity feedback loop (inner loop), and a position feedback loop. The velocity feedback adds extra damping to the system at all frequencies. This will result in a slower system and is therefor not recommended to use.[1] The position controller used is a Proportional-Integral controller. This controller does not provide higher gain at high frequencies to increase the bandwidth. Figure 12.8 shows the closed loop frequency response and the sensitivity of the resulting system with controller parameters used as implemented in practice. The system bandwidth is approximately 8 [Hz]. The obtained gain margin is only 2 [dB], which is very small. With only small process deviations, the closed loop system could become unstable.

To find a more robust and optimal controller H_c for this system, a lot of techniques are available. In practise the Proportional-Integral-Derivative or lead-lag controller is widely used. The transfer function of this controller is

$$H_l = k\frac{\alpha\tau_I s + 1}{\tau_I s + 1}\frac{\beta\tau_D s + 1}{\tau_D s + 1} \tag{12.4}$$

where $\alpha < 1$ (lag) and $\beta > 1$ (lead). The lag compensation is used to increase the DC gain to reduce the steady state error. The time constant τ_I is chosen large to obtain a pole close to the origin. α is chosen such that it leaves the closed loop system undisturbed in the neighborhood of the cross-over frequency, where the most critical stability margins are. The lead compensation is used to increase the bandwidth of the closed loop system. τ_D and *beta* must be chosen such that the desired bandwidth is reached. To reduce the effect of the process resonances, the controller can be extended with a notch filter to reduce the controller

---

[1] Compensation with a velocity feedforward would result in a Differential controller.

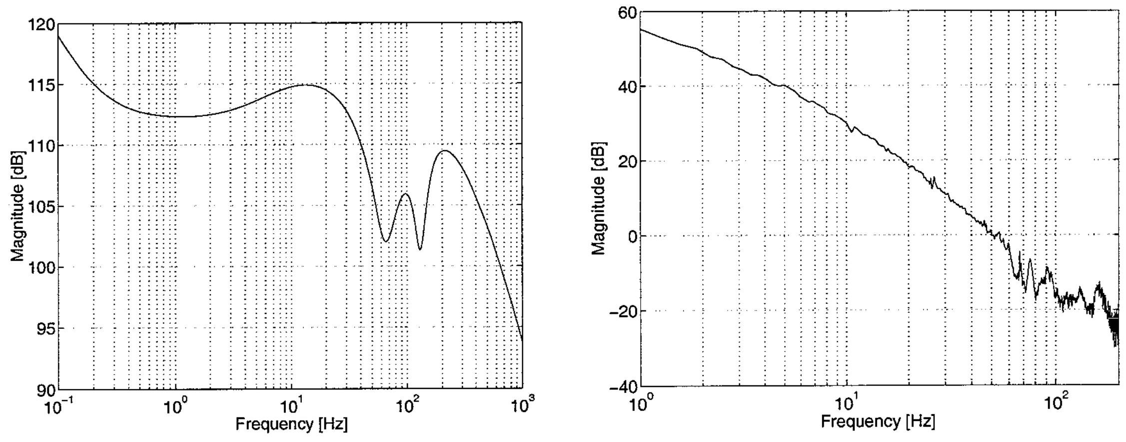

(a) Controller

(b) Open loop

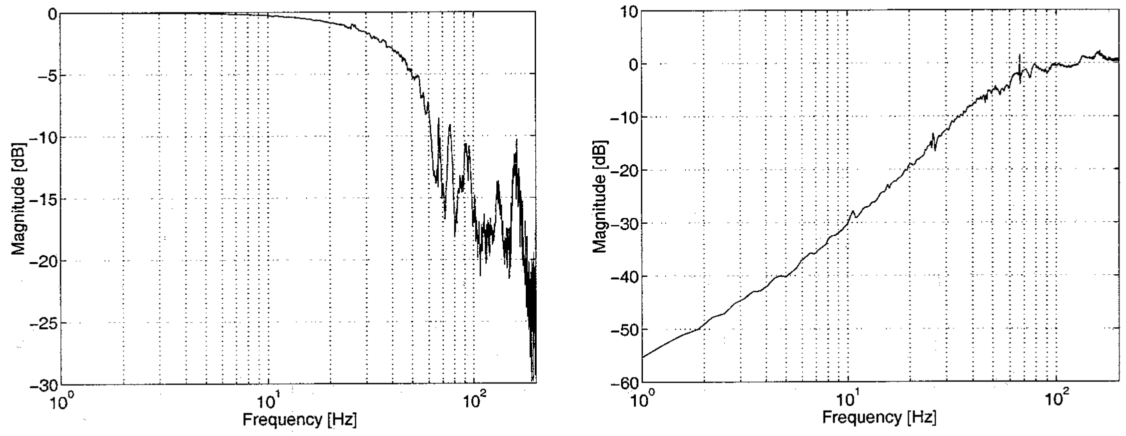

(c) Closed loop

(d) Sensitivity

Figure 12.9: Transfer functions with lead-lag controller

gain at these frequencies. The notch transfer function is

$$H_n = \frac{s^2 + 2\zeta_z \omega_n s + \omega_n^2}{s^2 + 2\zeta_p \omega_n s + \omega_n^2} \tag{12.5}$$

This creates a notch at frequency ω_n [rad/s]. The ratio between the damping ζ_z and ζ_p is a measure of the size of the notch. At the notch frequency, the gain is $|H_n| = \frac{(1+\zeta_z)}{(1+\zeta_p)}$, at frequencies $\omega \ll \omega_n$ and $\omega \gg \omega_n$, the gain is 1. The gain reduction introduced at the notch is thus $\frac{\zeta_z}{\zeta_p}$. To obtain a high roll-off rate at frequencies larger that the desired bandwidth, a low-pass filter can be used.

With these controller and filters, a closed loop bandwidth of 50 [Hz] can be easily obtained at the Linear Drive Unit. Figure 12.9(a) shows a bode plot of a lead-lag controller with two notches and a 2^{nd} order low pass filter. The resulting closed loop system (controller applied to the measured plant FRF) is shown in figure 12.9(c). The obtained bandwidth is 52 [Hz], with a gain margin of 11 [dB] and a phase margin of 60 [deg]. We see that the system is less sensitive to disturbances and process variations. To further optimize the performance, in addition to feedback a feedforward controller H_{ffw} can be used. The torque to be delivered by the motor can be computed by using the inverse of the process transfer function. Often an approximation

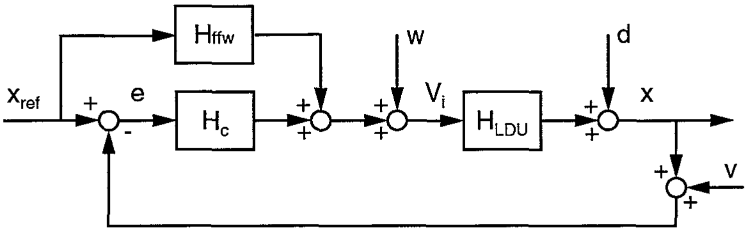

Figure 12.10: Optimized LDU controller

of H_{LDU} is used to simplify this computed torque controller. Also disturbances like friction can be taken into account using feedforward compensation. A feedforward controller does not affect the stability of the closed loop system. The optimized control scheme is presented in figure 12.10.

Chapter 13

Conclusions and recommendations

The analysis of the Linear Drive Unit has shown that the indirect measurement of the printhead position used, has direct effect on the image quality. The color spectrum of a grey-image shows significant correlation with the spectrum of the measurement error. This measurement error is introduced by the LDU mechanics. The capstan radius, the encoder mounting eccentricity and the encoder bearing eccentricity introduce ±18.8 [mm] patterns, which is the circumference of the capstan. The guide bar strip can also introduce periodic patterns. At the research machine these wavelengths were 150 and 300 [mm]. Dirt at the system has a similar effect on the measurement error as a deviation of the capstan assembly or guide bar. All slip in the system causes a direct measurement error, and therefor affects the image quality. It does however not directly mean that a deviation in the mechanics introduce a direct measurement error. Because of the interaction of these errors, these can amplify or weaken each other.
The error can be eliminated in various ways. One way is to increase all mechanical requirements, like the roundness of the capstan. This is however very costly and probably not practical realizable. A second method is to use the color spectrum measurement to calculate the expected positioning error and correct the measurement for this. This is however only possible for the patterns introduced by the capstan assembly, because only this wavelength is known within certain margins. A disadvantage of this method is that the effect of dirt, slip and varying guide bar thickness would still have effect on the image quality. The third, and most obvious method, is to directly measure the absolute position of the printheads using a linear encoder. The only measurement error left is the accuracy of the encoder, and thus all phenomenon described have no effect on the image quality.
The choice of whether to optimize the measurement is based on investment costs and profits, and is left for further research at Stork Digital Imaging.

The identified input-output relation between the Linear Drive Unit input V_i and output x shows several damped resonances, which can not be directly reduced to the (anti-)resonances found in the white box model. Up to 50 [Hz], the white box model gives a good approximation of the LDU and can be used for analysis. Optimization of the input-output relation shows that, theoretically, the highest process gain is obtained when the capstan radius is increased to $R_c = 6.2$ [mm] and the transmission wheel radius is decreased to $R_t = 23$ [mm]. Identification measurements with different capstan and transmission reel radii should find the practical optimal values.
The use of friction wheels put a large limitation on the performance of the LDU, as the

maximum allowable motor torque is decreased significantly. Now, slip occurs when the motor delivers a torque larger than 2.5 [mNm]. The pressure force of the capstan against the guide bar strip should be increased to 125 [N] to eliminate slip.

At the LDU the friction can be modelled by Coulomb friction only. It does not show a signification viscous friction level, nor stiction for small displacement near zero velocity. Because friction acts as a disturbance on the process, and increases the steady state error, it must be taken into account. With increasing weight of the LDU, the stiction regime is likely to increase, and when redesigning the system also this phenomenon can significantly limit the performance.

The present controller can be divided into two parts. The first part is a velocity feedback, which only adds extra damping to the system. This results in a slower system and is therefor not recommended to use. The position controller used is a Proportional-Integral controller, which provide high gain at low frequencies to decrease the steady state error, but not at high frequencies to increase the bandwidth. The closed loop system is close to instability. With a lead-lag controller with notches at the resonance frequencies and a low-pass filter to reduce high frequent measurement noise, a more robust closed loop system can be obtained with a higher bandwidth and smaller sensitivity. Using a computed torque controller and feedforward friction compensation can further optimize the performance.

References

[1] R.A.Benschop
Fast Access in Tape Drive Systems.
Natlab Technical Note Nr. 255/95, Eindhoven (1995)

[2] The Mathworks, Inc.
Real Time Workshop.
Natick, Massachusetts, USA, (1999)

[3] The Mathworks, Inc.
Target Language Compiler Reference Guide.
Natick, Massachusetts, USA, (1999)

[4] National Instruments.
AT-MIO E Series User Manual.
Austin, Texas, USA, (1994)

[5] National Instruments.
Ni-Daq Function Reference Manual for PC compatibles.
Austin, Texas, USA (1999)

[6] Precision Engineering.
Constructiepricipes 1.
TUE, Eindhoven (1997)

[7] R.H.A. Hensen, M.J.G. v.d. Molengraft and M. Steinbuch
Frequency domain identification of dunamic friction model parameters.
To appear in IEEE Transactions on Control Systems Technology.

[8] P.R.Bélanger.
Control Engineering: A Modern Approach.
Saunders College Publishing, Orlando, Florida, USA (1995)

Appendix A

Parameter values

This table shows the parameters used in simulation and identified as described in chapter 8.1. For the parameters which depend on the reel radii, we use $R_1 = 40$ [mm] and $R_2 = 20$ [mm].

parameter	**simulation**	**identified**	**description**	**units**
$c_1 = c_2$	1.0e2	4.5e2	spring constant paper	[N/m]
$c_{m1} = c_{m2}$	8.0e1	1.2e1	torsion spring constant motor shaft	[Nm]
$k_1 = k_2$	1.0e1	1.25e1	damping constant paper	[Ns/m]
$k_{m1} = k_{m2}$	1.0e-5	1.3e-2	torsion damping constant motor shaft	[Nms]
$J_{m1} = J_{m2}$	7.5e-4	1.5e-3	Inertia DC motor	[kgm^2]
J_1	2.4e-4	1.9e-4	Inertia reel & paper roll 1	[kgm^2]
J_2	1.0e-5	8.2e-6	Inertia reel & paper roll 2	[kgm^2]
$J_{10} = J_{20}$	1.0e-5	1.0e-6	Inertia reel & paper roll 2	[kgm^2]
J_c	5.0e-6	5.0e-6	Inertia capstan	[kgm^2]
ρ_{tape}	1.7e3	1.7e3	mass density paper	[kg/m^3]
h_{tape}	3.7e-2	3.7e-2	tape height	[m]
d_{tape}	0.5e-3	0.5e-3	tape thickness	[m]
m_1	2.3e-1	2.0e-2	reel mass	[kg]
m_2	0	0.2e-3	reel mass	[kg]
$K_{m1} = K_{m2}$	6.1e-2	6.1e-2	Motor constant 1	[Nm/A]
R_1	4.0e-2	3.8e-2	radius paper roll 1	[m]
R_2	2.0e-2	2.2e-2	radius paper roll 2	[m]
R_{min}	2.0e-2	2.0e-2	minimum radius paper rolls	[m]
R_c	1.25e-2	1.25e-3	radius capstan	[m]
T_s	0	0.002	sample time	[s]
$\tau_{F1} = \tau_{F2}$	1e-3	2.4e-3	Friction force	[Nm]

Appendix B

Simulink models

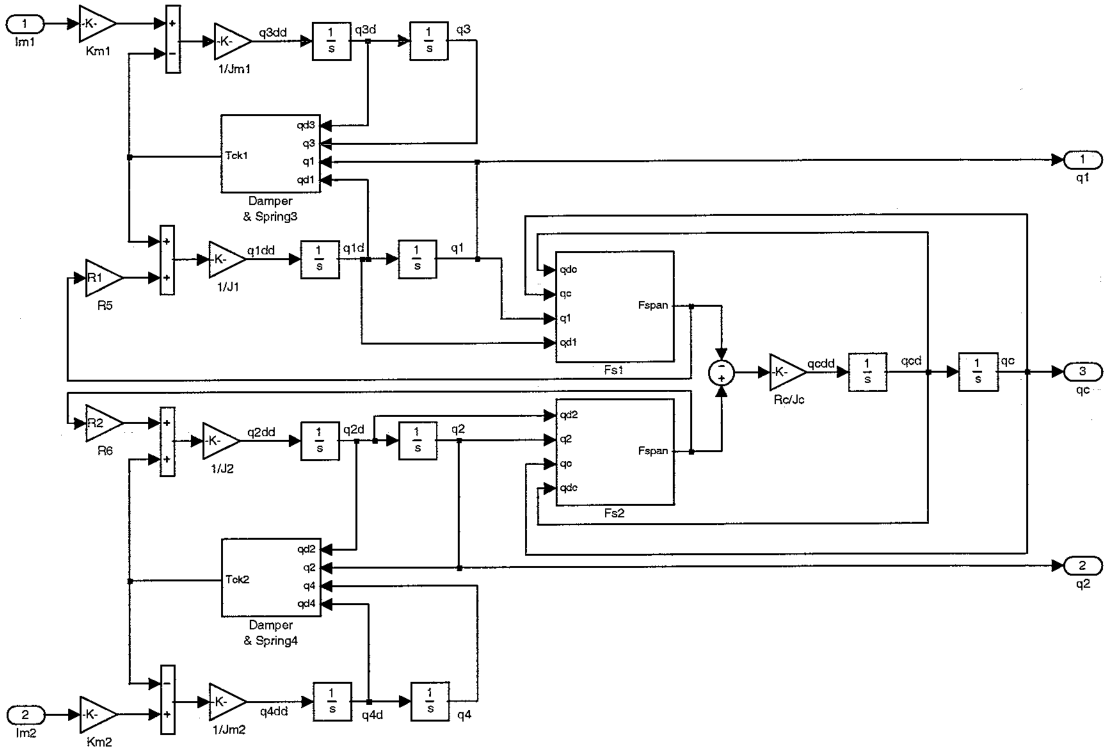

Figure B.1: Simulink model of the main process

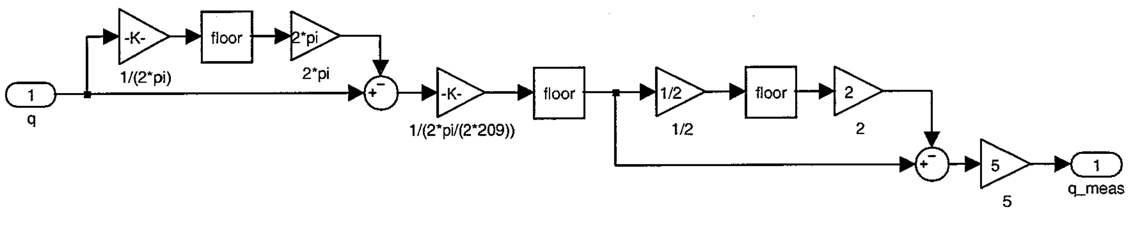

Figure B.2: Optical Sensor

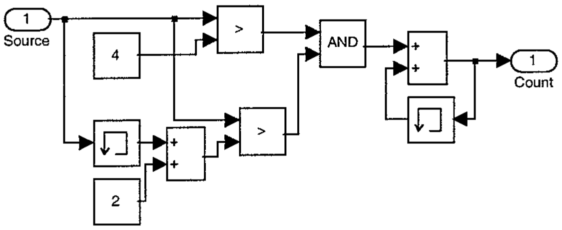

Figure B.3: Counter

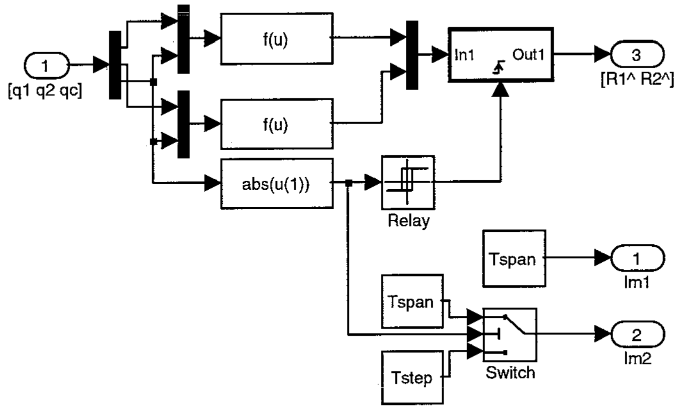

Figure B.4: Simulink model of initialization procedure

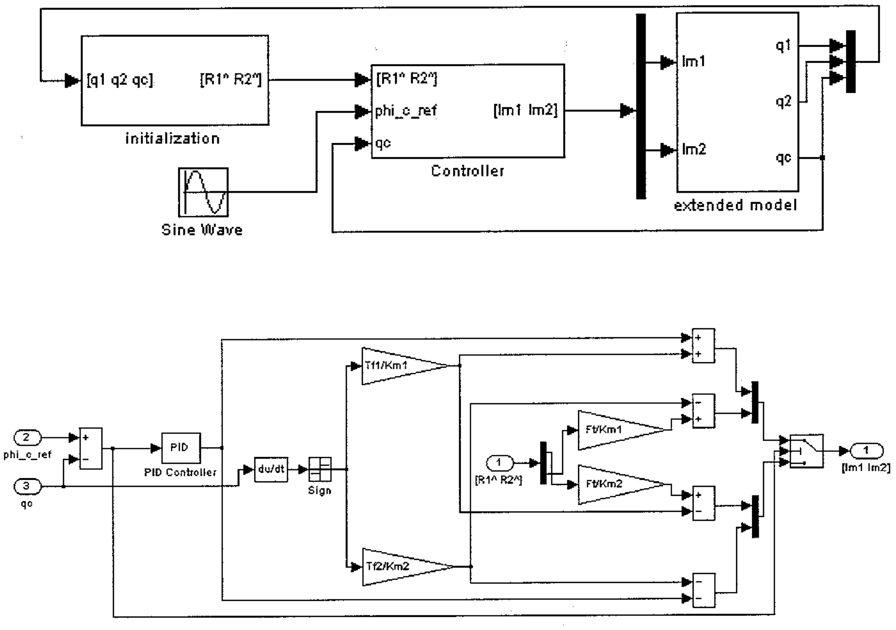

Subsystem 'Controller'

Figure B.5: Controller Simulink scheme

Appendix C

L292 electrical circuit

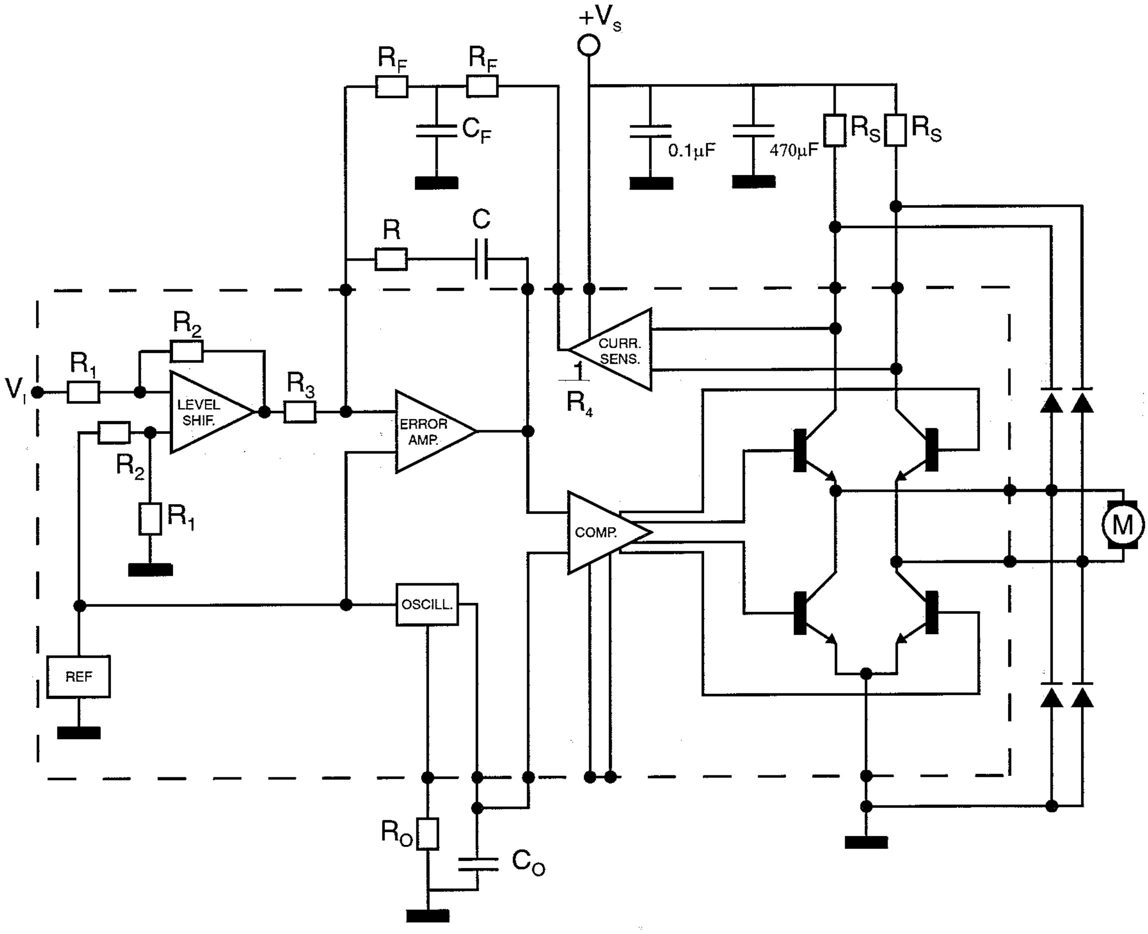

Figure C.1: L292 electrical circuit

Appendix D

Data Acquisition

In this appendix a detailed description is given of all the files and steps needed to generate and run the real-time code. We first start with an overview of all files.

`ATMIO16DE.c`	S-function driver used to communicate with the Simulink driver block
`ATMIO16DE.dll`	mex file of `ATMIO16DE.c`
`ATMIO16DE.mdl`	Simulink model with driver block
`ATMIO16DE.tlc`	inlined S-function driver used in code generation
`NIDAQ.h`	Nidaq header file
`NIDAQCNS.h`	Nidaq header file
`NIDAQ32.lib`	Nidaq library file
`NIDEX32.lib`	Nidaq library file
`RTSETUP.m`	m-script used for setting all model parameters
`RTBUILD.m`	m-script which starts the building process
`RTSTART.m`	m-script used to start the real-time executable

These files all have to be installed in the `MATLAB_ROOT\NIDAQ` directory and must be added to the Matlab path. To use these files, Nidaq 6.9 and Wintarget 2.0 must be installed on the system, together with Matlab r12, Real-Time Workshop and the Matlab LCC-compiler from the Mathworks. An other compiler may also be used, but then the libraries have to be converted. With Wintarget `wt_lcc.tmf` is supplied. This is the target make file used in code generation. To run properly, `$(MATLAB_ROOT)\nidaq\nidaq32.lib` must be added to the S-function libraries `S_FUNCTIONS_LIB` in this file. For Visual C users, the file `wt_vc.tmf` must be changed accordingly.

We will now give a full description of all files summarized above, except for the Nidaq files, and start with the Driver block.

Simulink Driver block

The driver block is a masked S-function. It calls `ATMIO16DE.dll` upon opening and closing. The parameters needed for setting up the DAQ board can be entered in the parameter list, these are described below.

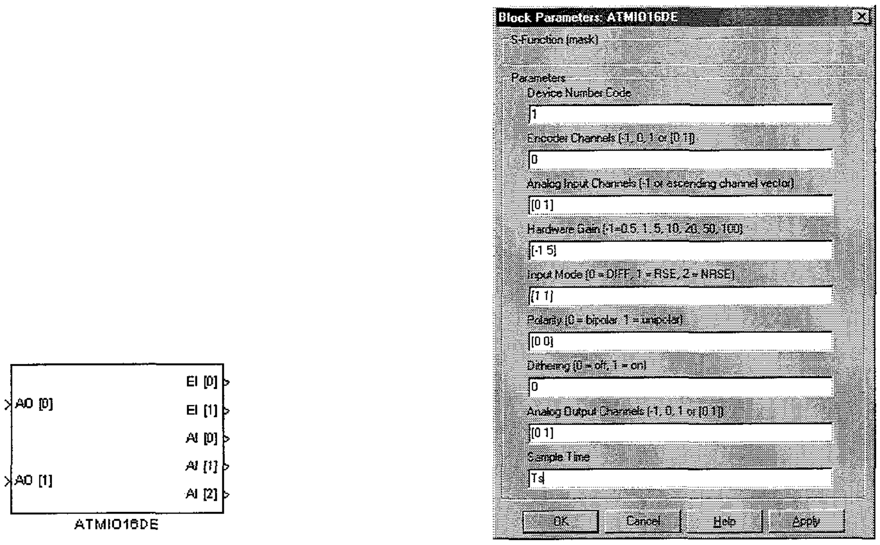

Block Parameters: ATMIO16DE
S-Function (mask)
Parameters
Device Number Code: 1
Encoder Channels (-1, 0, 1 or [0 1]): 0
Analog Input Channels (-1 or ascending channel vector): [0 1]
Hardware Gain (-1=0.5, 1, 5, 10, 20, 50, 100): [-1 5]
Input Mode (0 = DIFF, 1 = RSE, 2 = NRSE): [1 1]
Polarity (0 = bipolar, 1 = unipolar): [0 0]
Dithering (0 = off, 1 = on): 0
Analog Output Channels (-1, 0, 1 or [0 1]): [0 1]
Sample Time: Ts

(a) Simulink block *(b) block parameters*

Figure D.1: Simulink driver block

`Device Number Code`	This number should correspond with the Nidaq device number.
`Encoder Channels`	An ascending vector of Encoder channels to be scanned. Set to -1 if no encoder channels have to be used.
`Analog Input Channels`	An ascending vector of Analog Input channels to be scanned. Set to -1 if no analog inputs have to be used.
`Hardware Gain`	Vector of hardware gains corresponding to analog input vector. If a gain of 0.5 is to be used, the value must be set to -1.
`Input Mode`	Vector of input modes corresponding to analog input vector. 0 = Differential, 1 = RSE, 2 = NRSE
`Polarity`	Vector of polarities corresponding to analog input vector. 0 = Bipolar, 1 = Unipolar
`Dithering`	Scalar value that disables (0) or enables (1) dithering. Dithering can not be set per channel.
`Analog Output Channels`	An ascending vector of Analog Output channels to be set. Set to -1 if no analog output channels have to be used.

ATMIO16DE.c

This c-code file is an S-function to be used with the driver block. It gets all parameters entered in the block, checks them for some conditions and passes these values to the inlined S-function upon program building. It also sets the number of output and input ports according to the number of channels to be used. The encoder channels are mapped to the first ports. When running simulation, it sinks the analog output and generates analog and encoder inputs, all zero-valued. Further examination is left to the reader, and we will only refer to the Real Time Workshop User's Guide [2]. Below the full code is presented.

```
#define S_FUNCTION_NAME ATMIO16DE
#define S_FUNCTION_LEVEL 2
```

```
#include "simstruc.h"

#ifndef MATLAB_MEX_FILE
#error "Fatal Error: ATMIO16DE.c can only be used to create C-MEX S-Function"
#endif

#define  NUM_S_FUNCTION_PARAMS      (9)
#define  DEVICE_NUMBER_PARAM        (ssGetSFcnParam(S,0))
#define  ENCCHANS_PARAM             (ssGetSFcnParam(S,1))
#define  AICHANS_PARAM              (ssGetSFcnParam(S,2))
#define  GAIN_PARAM                 (ssGetSFcnParam(S,3))
#define  INPUTMODE_PARAM            (ssGetSFcnParam(S,4))
#define  POLARITY_PARAM             (ssGetSFcnParam(S,5))
#define  DITHER_PARAM               (ssGetSFcnParam(S,6))
#define  AOCHANS_PARAM              (ssGetSFcnParam(S,7))
#define  SAMPLE_TIME_PARAM          (ssGetSFcnParam(S,8))

#define  DEVICE_NUMBER              ((real_T) (mxGetPr(DEVICE_NUMBER_PARAM)[0]))
#define  ENCCHANS                   (mxGetPr(ENCCHANS_PARAM))
#define  AICHANS                    (mxGetPr(AICHANS_PARAM))
#define  GAIN                       (mxGetPr(GAIN_PARAM))
#define  INPUTMODE                  (mxGetPr(INPUTMODE_PARAM))
#define  POLARITY                   (mxGetPr(POLARITY_PARAM))
#define  DITHER                     ((real_T) mxGetPr(DITHER_PARAM)[0])
#define  AOCHANS                    (mxGetPr(AOCHANS_PARAM))
#define  SAMPLE_TIME                ((real_T) (mxGetPr(SAMPLE_TIME_PARAM)[0]))

#define  NUM_ENC                    mxGetNumberOfElements(ENCCHANS_PARAM)
#define  NUM_AI                     mxGetNumberOfElements(AICHANS_PARAM)
#define  NUM_AO                     mxGetNumberOfElements(AOCHANS_PARAM)

#include "nidaq.h"

#define MDL_CHECK_PARAMETERS
static void mdlCheckParameters(SimStruct *S)
{
    static char_T errMsg[256];
    boolean_T allParamsOK = 1;

    if (mxGetNumberOfElements(SAMPLE_TIME_PARAM) != 1) {
        sprintf(errMsg, "Sample Time must be a positive scalar.\n");
        allParamsOK = 0;
        goto EXIT_POINT;
    }
    if (mxGetNumberOfElements(AICHANS_PARAM) == 0) {
        sprintf(errMsg, "If no analog inputs should be used enter -1.");
        allParamsOK = 0;
        goto EXIT_POINT;
    }
    if (mxGetNumberOfElements(ENCCHANS_PARAM) == 0) {
        sprintf(errMsg, "If no encoders should be used enter -1.");
        allParamsOK = 0;
        goto EXIT_POINT;
    }
    if (mxGetNumberOfElements(AOCHANS_PARAM) == 0) {
        sprintf(errMsg, "If no analog ouputs should be used enter -1.");
```

```
        allParamsOK = 0;
        goto EXIT_POINT;
    }
  if (AICHANS[0] <0)
    return;
  else{
    if (mxGetNumberOfElements(GAIN_PARAM) != NUM_AI) {
        sprintf(errMsg, "Hardware Gain must have %i parameters.\n",NUM_AI);
        allParamsOK = 0;
        goto EXIT_POINT;
    }
    if (mxGetNumberOfElements(INPUTMODE_PARAM) != NUM_AI) {
        sprintf(errMsg, "Hardware Gain must have %i parameters.\n",NUM_AI);
        allParamsOK = 0;
        goto EXIT_POINT;
    }
    if (mxGetNumberOfElements(POLARITY_PARAM) != NUM_AI) {
        sprintf(errMsg, "Hardware Gain must have %i parameters.\n",NUM_AI);
        allParamsOK = 0;
        goto EXIT_POINT;
    }
    if (mxGetNumberOfElements(DITHER_PARAM) != 1) {
        sprintf(errMsg, "Hardware Gain must have 1 parameters.\n");
        allParamsOK = 0;
        goto EXIT_POINT;
    }
  }
  if (AOCHANS[0] <0){
    if (mxGetNumberOfElements(AOCHANS_PARAM) > 1) {
        sprintf(errMsg, "Analog output channels must be either 0, 1 or [0 1].
        If no analog output should be used enter -1.\n");
        allParamsOK = 0;
        goto EXIT_POINT;
    }
  }
  if (ENCCHANS[0] <0){
    if (mxGetNumberOfElements(ENCCHANS_PARAM) > 1) {
        sprintf(errMsg, "Encoder channels must be either 0, 1 or [0 1].
        If no encoder should be used enter -1.\n");
        allParamsOK = 0;
        goto EXIT_POINT;
    }
  }
    EXIT_POINT:
    if ( !allParamsOK ) {
        ssSetErrorStatus(S, errMsg);
    }
}
```

```
static void mdlInitializeSizes(SimStruct *S)
{
    ssSetNumSFcnParams(S, NUM_S_FUNCTION_PARAMS);
    #if defined(MATLAB_MEX_FILE)
        if ( ssGetNumSFcnParams(S) == ssGetSFcnParamsCount(S) ) {
            mdlCheckParameters(S);
            if ( ssGetErrorStatus(S) != NULL ) {
                return;
```

```
            }
        } else {
            return;
        }
    #endif
    {
        int_T i;
        for (i=0; i < NUM_S_FUNCTION_PARAMS; i++) {
            ssSetSFcnParamNotTunable(S, i);
        }
    }
  if (AOCHANS[0] <0){
    if ( !ssSetNumInputPorts(S, 0) ) return;
    }
  if (AOCHANS[0] >=0){
    if ( !ssSetNumInputPorts(S, NUM_AO) ) return;
    }
    {
        int_T iPort;
        for (iPort = 0; iPort < ssGetNumInputPorts(S); iPort++) {
            ssSetInputPortWidth(S, iPort, 1);
        }
    }
  if (AICHANS[0] <0 && ENCCHANS[0] <0){
      if ( !ssSetNumOutputPorts(S, 0) ) return;
      }
  if (AICHANS[0] <0 && ENCCHANS[0] >=0){
      if ( !ssSetNumOutputPorts(S, NUM_ENC) ) return;
    }
  if (AICHANS[0] >=0 && ENCCHANS[0] <0){
      if ( !ssSetNumOutputPorts(S, NUM_AI) ) return;
    }
  if (AICHANS[0] >=0 && ENCCHANS[0] >=0){
      if ( !ssSetNumOutputPorts(S, NUM_AI + NUM_ENC) ) return;
    }
    {
       int_T oPort;
       for (oPort = 0; oPort < ssGetNumOutputPorts(S); oPort++) {
            ssSetOutputPortWidth(S, oPort, 1);
       }
    }
    ssSetNumSampleTimes( S, 1);
}

static void mdlInitializeSampleTimes(SimStruct *S)
{
    ssSetSampleTime(S, 0, SAMPLE_TIME);
    ssSetOffsetTime(S, 0, 0.0);
}

#define MDL_START
static void mdlStart(SimStruct *S)
{
    if (ssGetSimMode(S) == SS_SIMMODE_NORMAL) {
        mexPrintf("\n The outputs of the DAQ-board block '%s' will be set "
                  "to zero during simulation in Simulink.\n", ssGetPath(S));
    }
```

```
}

static void mdlOutputs(SimStruct *S, int_T tid)
{
    int oPort;

    for (oPort = 0; oPort < ssGetNumOutputPorts(S); oPort++) {
        real_T *y = ssGetOutputPortRealSignal(S, oPort);
        y[0] = 0.0;
    }
}

static void mdlTerminate(SimStruct *S)
{
}

#define MDL_RTW
static void mdlRTW(SimStruct *S)
{
    if ( !ssWriteRTWParamSettings(S, 8,
                       SSWRITE_VALUE_VECT,  "EncChans", ENCCHANS, NUM_ENC,
                       SSWRITE_VALUE_VECT,  "AOChans", AOCHANS, NUM_AO,
                       SSWRITE_VALUE_VECT,  "AIChans", AICHANS, NUM_AI,
                       SSWRITE_VALUE_VECT,  "Gain", GAIN, NUM_AI,
                       SSWRITE_VALUE_VECT,  "InputMode", INPUTMODE, NUM_AI,
                       SSWRITE_VALUE_VECT,  "Polarity", POLARITY, NUM_AI,
                       SSWRITE_VALUE_NUM,   "DeviceNumber", DEVICE_NUMBER,
                       SSWRITE_VALUE_NUM,   "Dither", DITHER
        )                        ) {
        return;
    }
}

#ifdef MATLAB_MEX_FILE
#include "simulink.c"
#else
#include "cg_sfun.h"
#endif
```

ATMIO16DE.tlc

This inlined c-code file describes three function `Start`, `Outputs` and `Terminate`. We use function from the Nidaq libraries. These function are namely highly optimized for timing and speed of execution.

`Start`, performed when starting the real-time executable, but prior to starting the execution time, initializes the DAQ card, sets the dithering, initializes the analog inputs to the parameters set in the driver block, sets the analog output to the internal bipolar 10 [V] reference and immediate update, and finally sets the counters to event-counting. The initial count is set to half the counter size, to avoid initial counter jumps (if the counter goes through zero downwards, or through 2^{24} upwards, the count jumps 2^{24} counts).

In `Outputs` the communication with the DAQ card is described. To increase execution speed and efficiency, care is taken to reduce the use of variables. First the encoders are read, then the analog inputs are scanned and finally the voltages are written to the analog outputs.

In `Terminate` the encoders are reset to zero and the analog output voltages are set to 0 [V]. Further examination of the code is left to the reader, and we will only refer to the Target Language Compiler Reference Guide [3]. Below the full code is presented.

```
%implements "ATMIO16DE" "C"

%function BlockTypeSetup(block, system) void
  %if !EXISTS("INCLUDE_NIDAQ_H")
    %assign ::INCLUDE_NIDAQ_H = 1
    %openfile buffer
    /* Include information about the I/O board */
    #include "c:\matlabr12\nidaq\nidaq.h"
    %closefile buffer
    %<LibCacheIncludes(buffer)>
  %endif
  %if !EXISTS("INCLUDE_NIDAQCNS_H")
    %assign ::INCLUDE_NIDAQCNS_H = 1
    %openfile buffer
    /* Include information about the I/O board */
    #include "c:\matlabr12\nidaq\nidaqcns.h"
    %closefile buffer
    %<LibCacheIncludes(buffer)>
  %endif
%endfunction %% BlockTypeSetup

%function Start(block, system) Output

  %assign aiChans       = SFcnParamSettings.AIChans
  %assign gain          = SFcnParamSettings.Gain
  %assign dither        = SFcnParamSettings.Dither
  %assign inputMode     = SFcnParamSettings.InputMode
  %assign polarity      = SFcnParamSettings.Polarity
  %assign numAI         = SIZE(aiChans,1)
  %assign chIdx = 0

  short deviceNumberCode;
  short AIChanVect[%<numAI>];
  short GainVect[%<numAI>];

  %% Initializing the DAQ board

  Init_DA_Brds(1, &deviceNumberCode);
      %%deviceNumberCode should be 37

  %%Dithering on/off
  MIO_Config(1,%<CAST("Number",dither)>,0);

  %%Configuring the analog input ports

  %foreach oPort = numAI
    AIChanVect[%<oPort>] = %<CAST("Number",aiChans[oPort])>;
    GainVect[%<oPort>] = %<CAST("Number",gain[oPort])>;
    AI_Configure(1,%<CAST("Number",aiChans[oPort])>,%<CAST("Number",
                 inputMode[oPort])>,0,%<CAST("Number",polarity[oPort])>,0);
  %endforeach
```

```
  SCAN_Setup(1,%<numAI>,AIChanVect,GainVect);

  %%Configuring both the analog output ports:
  %%Bipolar, Internal reference 10V and Update when written to
  AO_Configure(1,0,0,0,10,0);
  AO_Configure(1,1,0,0,10,0);

  %%Configuring the counters for use with an encoder
  GPCTR_Control(1,ND_COUNTER_0,ND_RESET);
  GPCTR_Control(1,ND_COUNTER_1,ND_RESET);
  GPCTR_Set_Application(1,ND_COUNTER_0,ND_SIMPLE_EVENT_CNT);
  GPCTR_Set_Application(1,ND_COUNTER_1,ND_SIMPLE_EVENT_CNT);
  %%Set hardare controlled up and down counting
  %%DIO line 6 for counter 0
  %%DIO line 7 for counter 1
  GPCTR_Change_Parameter(1,ND_COUNTER_0,ND_UP_DOWN,ND_HARDWARE);
  GPCTR_Change_Parameter(1,ND_COUNTER_1,ND_UP_DOWN,ND_HARDWARE);
  GPCTR_Change_Parameter(1,ND_COUNTER_0,ND_INITIAL_COUNT,8388608);
  GPCTR_Change_Parameter(1,ND_COUNTER_1,ND_INITIAL_COUNT,8388608);
  GPCTR_Control(1,ND_COUNTER_0,ND_PROGRAM);
  GPCTR_Control(1,ND_COUNTER_1,ND_PROGRAM);

%endfunction %% Start

%function Outputs(block, system) Output

  %assign encChans      = SFcnParamSettings.EncChans
  %assign aiChans       = SFcnParamSettings.AIChans
  %assign numAI         = SIZE(aiChans,1)
  %assign numEnc        = SIZE(encChans,1)
  %assign aoChans       = SFcnParamSettings.AOChans
  %assign numAO         = block.NumDataInputPorts

  %if CAST("Number",aiChans[0]) >= 0
    double readings[%<numAI>];
  %else
  %endif

  %if CAST("Number",encChans[0]) >= 0
    unsigned long Enc_out[%<numEnc>];
  %else
  %endif

  %if CAST("Number",aiChans[0]) >= 0
    AI_VRead_Scan(1, readings);
  %else
  %endif

  %if CAST("Number",encChans[0]) >= 0
    %if numEnc == 1
      %if CAST("Number",encChans[0]) == 0
        GPCTR_Watch(1,ND_COUNTER_0,ND_COUNT,&Enc_out[0]);
      %else
        GPCTR_Watch(1,ND_COUNTER_1,ND_COUNT,&Enc_out[0]);
      %endif
    %else
      GPCTR_Watch(1,ND_COUNTER_0,ND_COUNT,&Enc_out[0]);
```

```
      GPCTR_Watch(1,ND_COUNTER_1,ND_COUNT,&Enc_out[1]);
    %endif
  %else
  %endif

  %if CAST("Number",aiChans[0]) >=0
    %if CAST("Number",encChans[0]) >=0
      %foreach oPort = numEnc
        %<LibBlockOutputSignal(oPort , "", "", 0)> = Enc_out[%<oPort>];
      %endforeach
      %foreach oPort = numAI
        %<LibBlockOutputSignal(oPort + numEnc, "", "", 0)> = readings[%<oPort>];
      %endforeach
    %elseif CAST("Number",encChans[0]) <0
      %foreach oPort = numAI
        %<LibBlockOutputSignal(oPort, "", "", 0)> = readings[%<oPort>];
      %endforeach
    %endif
  %elseif CAST("Number",aiChans[0]) <0
    %if CAST("Number",encChans[0]) >=0
      %foreach oPort = numEnc
        %<LibBlockOutputSignal(oPort, "", "", 0)> = Enc_out[%<oPort>];
      %endforeach
    %elseif CAST("Number",encChans[0]) <0
    %endif
  %endif

  %if CAST("Number",aoChans[0]) >= 0
    %foreach iPort = numAO
      AO_VWrite (1, %<CAST("Number",aoChans[iPort])>,
                 %<LibBlockInputSignal(iPort, "", "", 0)>);
    %endforeach
  %else
  %endif

%endfunction %% Output

%function Terminate(block, system) Output

  AO_VWrite (1, 0, 0);
  AO_VWrite (1, 1, 0);
  GPCTR_Control(1,ND_COUNTER_0,ND_RESET);
  GPCTR_Control(1,ND_COUNTER_1,ND_RESET);

%endfunction %% Terminate
%% EOF: ATMIO16DE.tlc
```

To give an idea of how the code is inlined in the final code to be executed, we show an example using 2 analog outputs, 3 analog inputs and 2 encoder channels. The written voltages are both `constant`, the inputs are plotted together in a scope. The Simulink model including the ATMIO16DE block is shown with the resulting c-code.

```
/*
 * example.c
 *
```

```
 * Real-Time Workshop code generation for Simulink model "example.mdl".
 *
 * Model Version                        : 1.0
 * Real-Time Workshop file version      : 4.0 $Date: 2000/09/19 19:45:27 $
 * Real-Time Workshop file generated on : Mon Oct 01 11:29:42 2001
 * TLC version                          : 4.0 (Aug 21 2000)
 * C source code generated on           : Mon Oct 01 11:29:42 2001
 *
 * Relevant TLC Options:
 *   InlineParameters      = 0
 *   RollThreshold         = 5
 *   CodeFormat            = RealTime
 *
 * Simulink model settings:
 *   Solver     : FixedStep
 *   StartTime  : 0.0 s
 *   StopTime   : 10.0 s
 *   FixedStep  : 0.01 s
 */

#include <math.h>
#include <string.h>
#include "example.h"
#include "example_prm.h"

/* Start of Functions in model "untitled" */

/* Start the model */
void MdlStart(void)
{
  short deviceNumberCode;
  short AIChanVect[3];
  short GainVect[3];

  Init_DA_Brds(1, &deviceNumberCode);

  MIO_Config(1,0,0);

  AIChanVect[0] = 0;
  GainVect[0] = -1;
  AI_Configure(1,0,1,0,0,0);
  AIChanVect[1] = 1;
  GainVect[1] = 5;
  AI_Configure(1,1,1,0,0,0);
  AIChanVect[2] = 2;
  GainVect[2] = 1;
  AI_Configure(1,2,1,0,1,0);

  SCAN_Setup(1,3,AIChanVect,GainVect);

  AO_Configure(1,0,0,0,10,0);
  AO_Configure(1,1,0,0,10,0);

  GPCTR_Control(1,ND_COUNTER_0,ND_RESET);
  GPCTR_Control(1,ND_COUNTER_1,ND_RESET);
  GPCTR_Set_Application(1,ND_COUNTER_0,ND_SIMPLE_EVENT_CNT);
  GPCTR_Set_Application(1,ND_COUNTER_1,ND_SIMPLE_EVENT_CNT);
```

```
  GPCTR_Change_Parameter(1,ND_COUNTER_0,ND_UP_DOWN,ND_HARDWARE);
  GPCTR_Change_Parameter(1,ND_COUNTER_1,ND_UP_DOWN,ND_HARDWARE);
  GPCTR_Change_Parameter(1,ND_COUNTER_0,ND_INITIAL_COUNT,8388608);
  GPCTR_Change_Parameter(1,ND_COUNTER_1,ND_INITIAL_COUNT,8388608);
  GPCTR_Control(1,ND_COUNTER_0,ND_PROGRAM);
  GPCTR_Control(1,ND_COUNTER_1,ND_PROGRAM);
}

/* Compute block outputs */
void MdlOutputs(int_T tid)
{
  double readings[3];
  unsigned long Enc_out[2];

  AI_VRead_Scan(1, readings);

  GPCTR_Watch(1,ND_COUNTER_0,ND_COUNT,&Enc_out[0]);
  GPCTR_Watch(1,ND_COUNTER_1,ND_COUNT,&Enc_out[1]);

      rtB.ATMIO16DE_o1 = Enc_out[0];
      rtB.ATMIO16DE_o2 = Enc_out[1];
      rtB.ATMIO16DE_o3 = readings[0];
      rtB.ATMIO16DE_o4 = readings[1];
      rtB.ATMIO16DE_o5 = readings[2];

  AO_VWrite (1, 0, (rtP.Constant_Value));
  AO_VWrite (1, 1, (rtP.Constant1_Value));
}

/* Perform model update */
void MdlUpdate(int_T tid)
{
    /* (no update code required) */
}

/* Terminate function */
void MdlTerminate(void)
{
  AO_VWrite (1, 0, 0);
  AO_VWrite (1, 1, 0);
  GPCTR_Control(1,ND_COUNTER_0,ND_RESET);
  GPCTR_Control(1,ND_COUNTER_1,ND_RESET);
}

/* End of Functions in model "example" */

#include "example_reg.h"

/* [EOF] example.c */
```

NIDAQ files

We will not detailed described the Nidaq files used, but only give a short description of the function used from the libraries. For further details we refer to the AT-MIO E Series user manual [4] and the Function Reference manual [5].

`Init_DA_Brds`	Initializes the DAQ board.
`MIO_Config`	Turns dithering on / off.
`SCAN_Setup`	Sets the scanning vector to the corresponding analog inputs and gains.
`AO_Configure`	Sets the polarity, reference and update mode of the analog outputs.
`GPCTR_Control`	Controls the operation of the general purpose counter. Used with parameter `ND_RESET`, it resets the counter and used with parameter `ND_PROGRAM`, it arms the counter.
`GPCTR_Set_Application`	Set the counter to count all events.
`GPCTR_Change_Parameter`	Set the counter Up/Down counting to be controlled by hardware.
`AI_VRead_Scan`	Reads the channels selected by `SCAN_SETUP` and scales the values to voltages.
`GPCTR_Watch`	Reads the counter value without affecting its operation.
`AO_VWrite`	Scales and writes the voltages to the analog outputs.

RTBuild.m

To generate the real-time code and to build the executable, the user can use `RTBuild.m`. This script first calls `RTSetup.m`, which sets all model parameters. Then the Real-Time Toolbox file `RTWbuild.m` is called, which start the building process. Once the executable is successfully build, compiled and linked, `RTStart.m` is called which starts the executable using the Wintarget `-w` option, which makes sure that the execution only starts when the real-time code is started within Simulink. `RTSetup.m` and `RTStart.m` can also be called independent of `RTBuild.m`. The three script files are shown below.

```
function rtbuild(Model)

%rtbuild.m
%
%usage      rtbuild('<Model>')
%
%1. Opens the model specified with <Model>.
%  With no input argument this applies to the current system.
%      (Be sure to activate the correct system)
%2. Sets the RTW parameters using rtsetup.m
%2. Builds the model for Wintarget.
%3. Starts real-time execution using rtstart.m

if nargin<1
   Model=get_param(0,'CurrentSystem')
else
   open_system(Model);
end

rtsetup(Model);
rtwbuild(Model);
rtstart(Model);
```

RTSetup.m

```
function rtsetup(Model)

%rtsetup.m
%
%usage      rtsetup('<Model>')
%   With no input argument this applies to the current system.
%       (Be sure to activate the correct system)
%
%1. Sets all block priorities to 1 and the ATMIO16DE block to -1.
%2. Sets all rtw paramaters for Wintarget real-time execution.

if nargin<1
    Model=get_param(0,'CurrentSystem')
else
    open_system(Model);
end

blocks=get_param(Model,'Blocks');

for i=1:size(blocks,1)
    if size(get_param(char(strcat(Model,'/',blocks(i))),'Virtual'),2) == 3
        set_param(char(strcat(Model,'/',blocks(i))),'Priority','1')
    else
    end
    if isfield(get_param(char(strcat(Model,'/',blocks(i))),'ObjectParameters'),
               'TreatAsAtomicUnit')
        set_param(char(strcat(Model,'/',blocks(i))),'TreatAsAtomicUnit','on')
        set_param(char(strcat(Model,'/',blocks(i))),'RTWSystemCode','inline')
        set_param(char(strcat(Model,'/',blocks(i))),'Priority','1')
    else
    end
end

set_param(char(strcat(Model,'/ATMIO16DE')),'Priority','-1')
set_param(Model,'SolverMode','SingleTasking')
set_param(Model,'SimulationMode','external')
set_param(Model,'Solver','ode5')

set_param(Model,'LoadExternalInput','off')
set_param(Model,'SaveTime','off')
set_param(Model,'SaveState','off')
set_param(Model,'SaveOutput','off')
set_param(Model,'LoadInitialState','off')
set_param(Model,'SaveFinalState','off')
set_param(Model,'LimitDataPoints','off')

set_param(Model,'RTWBuildArgs','EXT_MODE=1')
set_param(Model,'RTWInlineParameters','off')
set_param(Model,'RTWRetainRTWFile','on')
set_param(Model,'RTWSystemTargetFile','wintarget.tlc')
set_param(Model,'RTWTemplateMakefile','wt_default_tmf')
set_param(Model,'RTWMakeCommand','make_rtw')
set_param(Model,'RTWGenerateCodeOnly','off')

set_param(Model,'TLCProfiler','off')
```

```
set_param(Model,'TLCDebug','off')
set_param(Model,'TLCCoverage','off')

set_param(Model,'BufferReuse','on')
set_param(Model,'ParameterPooling','on')
set_param(Model,'BlockReductionOpt','on')
set_param(Model,'BooleanDataType','on')
```

RTStart.m

```
function rtstart(Model)

%rtstart.m
%
%usage      rtstart('<Model>')
%
%1. Opens the model specified with <Model>.
%   With no input argument this applies to the current system.
%       (Be sure to activate the correct system)
%2. Starts real-time execution using wtstartup -w
%   (sets the executable to wait for real-time code start)
if nargin<1
    Model=get_param(0,'CurrentSystem');
else
    open_system(Model);
end

wt_startup(strcat(Model,' -w'))
```

Appendix E

DC Motor specifications

IC34 Iron Core DC gear motor 0.6 Nm

Dimensional drawing

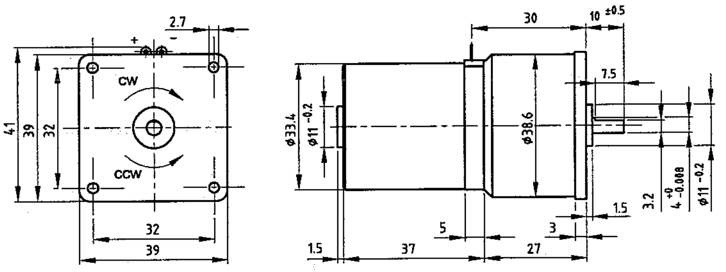

Gear Motor data

Gear motor Order number			Gear ratio	Direction of rotation	Nominal voltage [V]	Maximal voltage [V]	Maximum torque continuous [Nm] (nominal load)	Maximum torque intermittent [Nm]	Speed at no load [rpm]	Speed at nominal load [rpm]	Current at no load [mA]	Current at nominal load [mA]	Maximal radial force [N]	Maximal axial force [N]
9904 120 53 +	406		81:1	cw	6	7.2	0.24	0.48	47.3	32.9	103	460	6	6
	606				12	14.4			45.3	35.6	48	215		
	706				24	28.8			45.4	35.8	24	108		
	407		150.4:1	ccw	6	7.2	0.45	0.8	25.5	16.8	103	502	8	8
	607				12	14.4			24.4	18.5	48	234		
	707				24	28.8			24.4	18.6	24	118		
	408		243:1	ccw	6	7.2	0.6	0.8	15.8	11.3	103	434	8	8
	608				12	14.4			15.1	12.1	48	204		
	708				24	28.8			15.1	12.2	24	101		
	409		451.25:1	cw	6	7.2	0.6	0.8	8.5	7.1	103	300	10	10
	609				12	14.4			8.1	7.1	48	140		
	709				24	28.8			8.1	7.2	24	70		
	411		729:1	cw	6	7.2	0.6	0.8	5.3	4.7	103	225	10	10
	611				12	14.4			5.0	4.6	48	105		
	711				24	28.8			5.0	4.7	24	53		

Motor data

	Nominal Voltage [V]	Rotor resist. [Ohm]	Speed at no load [rpm]	Stall torque [mNm]	Torque const. [mNm/A]
9904 120 534..	6	3.6	3800	23	14
9904 120 536..	12	15	3550	23	30
9904 120 537..	24	58	3550	23	61

General data

*	Type of bearings	sleeve	
*	Commutation system	graphite / copper	
*●	Gear material	plastic / metal	
*	Axial play	0.5	mm
*	Ambient temp. range operating	-20/+60	°C
*	Ambient temp. range storage	-40/+70	°C
*●	Thermal resistance winding–ambient	30	K/W
*●	Mass of gear motor	125	g

Appendix F

Linear Drive Unit Model

The motor, transmission wheel and encoder are modelled as rotating bodies with inertia I_m, I_t and I_e respectively. The motor shaft is modelled as a rotational spring/damper with stiffness k_s and damping b_s with a rotating body at the end. The inertia of this body is negligible. The capstan is modelled as two rotational spring/dampers with stiffness k_c and damping b_c, and a body with a inertia I_c in the middle. The friction due to the bearing of the capstan is modelled as viscous friction B_c at the capstan. The complete unit is modelled as a translating mass M, which is connected rigid to the capstan and is subjected to viscous friction B_m. The motor shaft, transmission wheel and the capstan are considered to have a radius R_s, R_t and R_c respectively. We neglect the internal friction of the motor and the encoder.

By using D'Alemberts laws at the system shown in figure 12.1, we can deduct the following model:

$$\begin{aligned}
K_{m1} I_m &= K_{m2}\dot{\theta}_m + \tau_m && \text{(F.1)}\\
\tau_m &= J_m\ddot{\theta}_m + b_s(\dot{\theta}_m - \dot{\theta}_s) + k_s(\theta_m - \theta_s) && \text{(F.2)}\\
b_s(\dot{\theta}_m - \dot{\theta}_s) + k_s(\theta_m - \theta_s) &= f_s R_s && \text{(F.3)}\\
f_s R_t &= J_t\ddot{\theta}_t + b_c(\dot{\theta}_t - \dot{\theta}_c) + k_c(\theta_t - \theta_c) && \text{(F.4)}\\
b_c(\dot{\theta}_t - \dot{\theta}_c) + k_c(\theta_t - \theta_c) &= J_c\ddot{\theta}_c + b_c(\dot{\theta}_c - \dot{\theta}_e) + k_c(\theta_c - \theta_e) + B_c\dot{\theta}_c + f_c R_c && \text{(F.5)}\\
f_c &= M\ddot{x} + B_m\dot{x} && \text{(F.6)}\\
b_c(\dot{\theta}_c - \dot{\theta}_e) + k_c(\theta_c - \theta_e) &= J_e\ddot{\theta}_e && \text{(F.7)}
\end{aligned}$$

Where K_{m1} is the motor torque constant, K_{m2} is the motor speed/torque gradient and I_m is the input current of the motor.

We consider the transmission between the motor shaft and the transmission wheel and between the capstan and guide bar strip ideal, and can therefor write:

$$\begin{aligned}
\theta_s &= N\theta_t && \text{(F.8)}\\
x &= R_c\theta_c && \text{(F.9)}
\end{aligned}$$

By using state vector $\mathbf{x} = [\theta_m \quad \dot{\theta}_m \quad \theta_t \quad \dot{\theta}_t \quad \theta_c \quad \dot{\theta}_c \quad \theta_e \quad \dot{\theta}_e]^T$, input $u = I_m$ and output $y = x$, we can write relation F.1 to F.9 in a state space model as

$$\begin{aligned}
\dot{\mathbf{x}} &= A\mathbf{x} + Bu && \text{(F.10)}\\
y &= C\mathbf{x} + Du && \text{(F.11)}
\end{aligned}$$

Where

$$\begin{aligned}
A &= \begin{bmatrix}
0 & 1 & 0 & 0 & 0 & 0 & 0 & 0 \\
-\frac{k_s}{J_m} & -\frac{b_s+K_{m2}}{J_m} & \frac{Nk_s}{J_m} & \frac{Nb_s}{J_m} & 0 & 0 & 0 & 0 \\
0 & 0 & 0 & 1 & 0 & 0 & 0 & 0 \\
\frac{Nk_s}{J_t} & \frac{Nb_s}{J_t} & -\frac{k_c+N^2k_s}{J_t} & -\frac{b_c+N^2b_m}{J_t} & 0 & 0 & & \\
0 & 0 & 0 & 0 & 0 & 1 & 0 & 0 \\
0 & 0 & \frac{k_c}{J_c+MR_c^2} & \frac{b_c}{J_c+MR_c^2} & -\frac{2k_c}{J_c+MR_c^2} & -\frac{2b_c+B_c+R_c^2B_m}{J_c+MR_c^2} & \frac{k_c}{J_c+MR_c^2} & \frac{b_c}{J_c+MR_c^2} \\
0 & 0 & 0 & 0 & 0 & 0 & 0 & 1 \\
0 & 0 & 0 & 0 & \frac{k_c}{J_e} & \frac{b_c}{J_e} & -\frac{k_c}{J_e} & -\frac{b_c}{J_e}
\end{bmatrix} \\
B &= [\, 0 \;\; \tfrac{K_{m1}}{J_m} \;\; 0 \;\; 0 \;\; 0 \;\; 0 \;\; 0 \;\; 0 \,]^T \\
C &= [\, 0 \;\; 0 \;\; 0 \;\; 0 \;\; R_c \;\; 0 \;\; 0 \;\; 0 \,]^T \\
D &= 0
\end{aligned}$$

parameter estimation

The rotational stiffness of a bar can be expressed as

$$k = \frac{\pi G R^4}{2l} \tag{F.12}$$

The inertia of a bar or wheel can be expressed

$$J = 1/2MR^2 \tag{F.13}$$

where

$$M = \pi R^2 l \rho \tag{F.14}$$

For parameter estimation we use the properties of normal steel, $G = 70 \cdot 10^9$ [Nm^{-2}], $\rho = 7.85 \cdot 10^3$ [kgm^{-3}]. The motor and encoder parameters are provided by the manufacturer. The table below gives a summation of the model parameters.

parameter	**value**	**description**	**units**
R_s	1.5e-3	radius motor shaft	[m]
R_t	3.0e-2	radius transmission wheel	[m]
R_c	3.0e-3	radius capstan	[m]
l_s	1.0e-3	length motor shaft	[m]
l_t	2.0e-3	thickness transmission wheel	[m]
l_c	1.0e-2	length capstan	[m]
k_s	1.0e1	torsion spring constant motor shaft	[Nm]
k_c	1.0e2	torsion spring constant capstan	[Nm]
J_m	1.0e-6	inertia DC motor	[kgm^2]
J_t	1.0e-5	inertia transmission wheel	[kgm^2]
J_c	1.0e-7	inertia capstan	[kgm^2]
J_e	3.0e-6	inertia encoder	[kgm^2]
M	5	total system weight	[kg]
K_{m1}	21e-3	motor constant	[Nm/A]
N	20	transmission ratio	[-]